Monthly Notices
of the
ROYAL ASTRONOMICAL SOCIETY

MNRAS **462,** 2046–2062 (2016)
Advance Access publication 2016 July 22

doi:10.1093/mnras/stw1790

Physical properties of galaxies: towards a consistent comparison between hydrodynamical simulations and SDSS

Giovanni Guidi,[1]★ Cecilia Scannapieco,[1] Jakob Walcher[1] and Anna Gallazzi[2]

[1]*Leibniz-Institut für Astrophysik Potsdam (AIP), An der Sternwarte 16, D-14482 Potsdam, Germany*
[2]*INAF–Osservatorio Astrofisico di Arcetri, Largo Enrico Fermi 5, I-50125 Firenze, Italy*

Accepted 2016 July 20. Received 2016 July 19; in original form 2016 February 19

ABSTRACT

We study the effects of applying observational techniques to derive the properties of simulated galaxies, with the aim of making an unbiased comparison between observations and simulations. For our study, we used 15 galaxies simulated in a cosmological context using three different feedback and chemical enrichment models, and compared their $z = 0$ properties with data from the Sloan Digital Sky Survey (SDSS). We show that the physical properties obtained directly from the simulations without post-processing can be very different from those obtained mimicking observational techniques. In order to provide simulators a way to reliably compare their galaxies with SDSS data, for each physical property that we studied – colours, magnitudes, gas and stellar metallicities, mean stellar ages and star formation rates – we give scaling relations that can be easily applied to the values extracted from the simulations; these scalings have in general a high correlation, except for the gas oxygen metallicities. Our simulated galaxies are photometrically similar to galaxies in the blue sequence/green valley, but in general they appear older, passive and with lower metal content compared to most of the spirals in SDSS. As a careful assessment of the agreement/disagreement with observations is the primary test of the baryonic physics implemented in hydrodynamical codes, our study shows that considering the observational biases in the derivation of the galaxies' properties is of fundamental importance to decide on the failure/success of a galaxy formation model.

Key words: hydrodynamics – radiative transfer – methods: numerical – galaxies: evolution – galaxies: formation – cosmology: theory.

1 INTRODUCTION

The various physical processes that occur at galactic scales during galaxy evolution leave imprints on the shape and features of the galaxies' spectral energy distributions (SEDs), which represent the main source of knowledge about the properties of galaxies in the Universe. Observational algorithms are able to recover, from a galaxy's SED, its physical properties such as the stellar, gas and metal content, the conditions of the interstellar medium (ISM) and the properties of active galactic nuclei (AGNs). These methods can provide constraints on different physical properties, either exploiting a pixel-by-pixel fit to the spectrum (e.g. Cappellari & Emsellem 2004; Cid Fernandes et al. 2005; Ocvirk et al. 2006; Walcher et al. 2015) or interpreting single or few spectral features, for instance the emission line luminosity (Kennicutt 1998), emission line ratios (Kobulnicky & Kewley 2004), Lick absorption indices (Gallazzi et al. 2005) or the 4000 Å break (Bruzual 1983).

With the advent of large surveys such as 2dFGRS, SDSS, 2MASS, ALMA, HUDF, DEEP2, *Spitzer*, *Herschel* (Colless 1999; Abazajian et al. 2003; Werner et al. 2004; Beckwith et al. 2006; Skrutskie et al. 2006; Pilbratt et al. 2010; Hodge et al. 2013; Newman et al. 2013), huge data sets of galaxy photometric and spectral information at different wavelengths and redshifts are now available to observers. Moreover, integral field unit (IFU) spectrographs (e.g. MUSE, Bacon et al. 2004; WEAVE, Dalton et al. 2014) are opening the possibility to study spatially resolved properties of nearby galaxies, and thanks to IFU surveys such as CALIFA (Sánchez et al. 2012; García-Benito et al. 2015), MANGA (Bundy et al. 2015) and SAMI (Allen et al. 2015), two-dimensional spectral maps of galaxies are now available, providing in turn a more comprehensive view of a galaxy's formation and evolution. The analysis of these large data sets enables astronomers to study the properties of galaxies in the Universe at different redshifts, and has allowed the derivation of important global quantities and relations, such as the cosmic star formation history (Madau & Dickinson 2014), the stellar mass function (Baldry et al. 2012; Song et al. 2015) and the mass–metallicity relation (Tremonti et al. 2004; Erb et al. 2006).

★E-mail: gguidi@aip.de

This wealth of data is also useful to test the results of hydrodynamical simulations of galaxy formation in cosmological context, which follow the linked evolution of gas and dark matter from the early stages of collapse (assuming recipes for star formation, supernovae and AGN feedback and chemical enrichment) and are able to connect the observed galaxy properties with a galaxy's merger and accretion history (e.g. Scannapieco et al. 2009, 2015; Oppenheimer et al. 2010; Naab et al. 2014; Nuza et al. 2014; Vogelsberger et al. 2014; Creasey et al. 2015; Nelson et al. 2015; Schaye et al. 2015). The results of hydrodynamical simulations have also been used recently to test and calibrate observational diagnostics, as they have the advantage that, unlike in observations, the physical properties of the galaxies are known a priori (Bellovary et al. 2014; Hayward et al. 2014; Michałowski et al. 2014; Hayward & Smith 2015; Smith & Hayward 2015). However, since the simulations contain information on the mass distributions, while observations are based on the analysis of the light emitted by galaxies, in general the various physical properties are differently defined in observational and simulation studies. For this reason, a simple comparison between them might not be reliable (e.g. Scannapieco et al. 2010), and a suitable conversion of simulations into mock observations is required in order to perform an unbiased comparison. The creation of mock observations of simulated galaxies is possible using different approaches, including radiative transfer computations that follow the generation and propagation of light in a dusty ISM (e.g. Jonsson, Groves & Cox 2010; Domínguez-Tenreiro et al. 2014).

In order to derive the galaxy properties from the mock SEDs, it is also important to take into account that each galaxy survey suffers from observational biases related to the observational setup and strategy, as well as from the different assumptions in the pipelines used to derive the physical properties (Walcher et al. 2011). The existence of these observational effects can have a strong influence in the comparison between simulations and observations, as it has already been shown that various methods to derive galaxy properties show large variations (Scannapieco et al. 2010; Michałowski et al. 2014; Hayward & Smith 2015; Smith & Hayward 2015).

In this paper, we study the effects of properly taking into account the observational biases when simulations are compared with data from the Sloan Digital Sky Survey (SDSS). For this, we mimic the derivation of galaxy properties done in SDSS, and consider the biases of this survey. In the companion paper Guidi, Scannapieco & Walcher (2015, hereafter Paper I), we discussed the models used to generate mock SEDs from 15 simulations that we use in our study, and we compared the results of applying different observational estimators on the values derived for the galaxies' colours, magnitudes, stellar masses, star formation rates (SFRs), gas and stellar metallicities and mean stellar ages. In particular, we focused on the ability of the observational methods to recover galaxy properties close to the ones calculated directly from the simulations without post-processing, and we made a detailed study on the biases and systematics of the different estimators.

We found in Paper I that biases and systematics affect all galaxy properties at different levels, and arise mainly from the specific design of the observational setup, from using mass-weighted or luminosity-weighted averaged quantities, from the different parametrization of the template of models fitted to the spectrum/photometry of a galaxy, and from the calibrations assumed to derive the gas metallicity and SFR. These results are used in this work, in which we focus on an unbiased comparison between the simulated galaxies and observations of SDSS.

The structure of the paper is as follows. In Section 2, we describe the simulations and the feedback and chemical models used to generate the galaxy sample, as well as the methods used to create the synthetic observations. In Section 3, we present the observational data set and we explain our selection of a subsample of type-classified galaxies. In Section 4, we compare the different physical properties of the simulated galaxies with SDSS, and we provide fitting functions to convert the values derived directly from the simulations into the ones extracted observationally. Finally, in Section 5, we give our conclusions.

2 METHODOLOGY

2.1 The simulations

We use in this work cosmological hydrodynamical simulations of galaxy formation that are based on the dark-matter-only Aquarius simulations (Springel et al. 2008). In particular, we use five galaxy haloes with present-day virial mass similar to the Milky Way, i.e. 0.7×10^{12} M$_\odot$ $< M_{200} < 1.7 \times 10^{12}$ M$_\odot$ (see Scannapieco et al. 2009 for details). Each of the five haloes is then re-simulated up to the present time including a baryonic component using the zoom-in technique (Tormen, Bouchet & White 1997), with three different hydrodynamical codes based on GADGET-3 (Springel 2005) which assume various recipes for star formation, chemical enrichment, metal-dependent cooling and supernova (SN) feedback, composing a total of 15 galaxies. As shown in Scannapieco et al. (2012), differences in the implementation of SN feedback have strong effects on the properties of simulated galaxies, and different hydrodynamical codes can produce galaxies with a large range of physical properties (e.g. morphologies, sizes, metallicities, ages, SFRs) even for the same dark-matter halo.

In order to identify the different galaxies, we assign letters from A to E for the five dark-matter haloes, adding a label for the hydrodynamical code with which the galaxies have been simulated: either CS, CS$^+$ or MA. Simulations CS are run with the model described in Scannapieco et al. (2005, 2006), which includes star formation, chemical enrichment, metal-dependent cooling, feedback from Type Ia and Type II supernova, and a multiphase model for the ISM. The second set of five simulations labelled CS$^+$ is generated with an updated version of the Scannapieco et al. (2005, 2006) model by Poulhazan et al. (in preparation), which adopts different choices for the chemical yields, a Chabrier initial mass function (IMF), and includes chemical feedback from asymptotic giant branch (AGB) stars. The third set, referred to as MA, is simulated with the update to the Scannapieco et al. code by Aumer et al. (2013); the main changes are a different set of chemical yields (which also include AGB stars), a different metal-dependent cooling function and a Kroupa IMF. In addition, the code has a different implementation of energy feedback from SNe, which is divided into a thermal and a kinetic part, and it includes feedback from radiation pressure coming from massive young stars. The MA model has in general stronger feedback compared to the CS/CS$^+$ models, resulting in more disky, younger galaxies. All the 15 galaxies of our sample have, at redshift $z = 0$, total stellar masses within 1–10 $\times$ 10^{10} M$_\odot$, gas masses in the range 3–10 $\times$ 10^{10} M$_\odot$, stellar/gas mass resolution of 2–5 $\times$ 10^5 M$_\odot$, dark-matter particle mass of 1–2 $\times$ 10^6 M$_\odot$ and gravitational softening of 300–700 pc. The cosmological parameters assumed are $\Omega_\mathrm{m} = 0.25$, $\Omega_\Lambda = 0.75$, $\Omega_\mathrm{b} = 0.04$, $\sigma_8 = 0.9$ and $H_0 = 100\,h$ km s^{-1} Mpc^{-1} with $h = 0.73$.

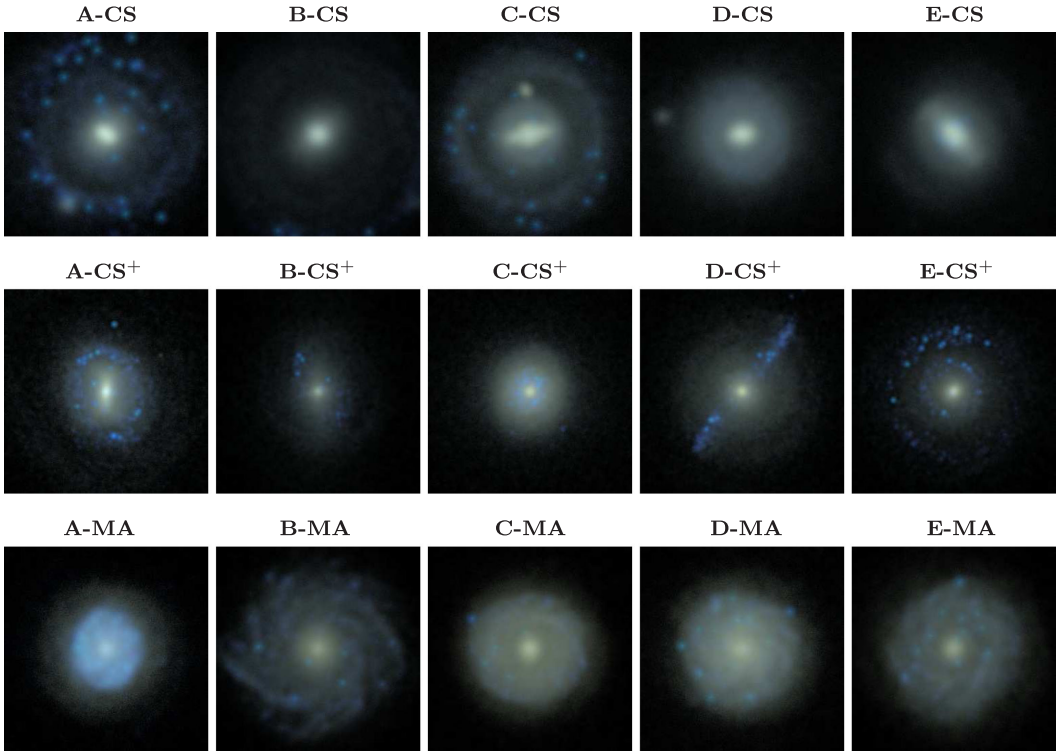

Figure 1. (u, r, z) multi-band face-on images of the 15 simulated galaxies, as predicted from the radiative transfer calculation of SUNRISE, for a 60 × 60 kpc field of view.

2.2 Creating the mock observations

The hydrodynamical simulations at redshift $z = 0$ have been post-processed with the radiative transfer code SUNRISE (Jonsson 2006; Jonsson et al. 2010), which simulates the propagation of light through a dusty ISM using Monte Carlo techniques, and self-consistently derives the spectra of the simulated galaxies from different observing positions, including stellar/nebular emission, dust absorption and IR emission. In a first stage, SUNRISE assigns each star particle a spectrum. For star particles older than 10 Myr, the stellar spectrum is selected according to the age, metallicity and mass of the particle from a template of spectra generated with the stellar population synthesis (SPS) code STARBURST99, choosing the Padova 1994 stellar tracks (Fagotto et al. 1994a,b), a Kroupa IMF (Kroupa 2002, with $\alpha = 1.3$ for $m_{\rm star} = 0.1$–$0.5\,{\rm M}_{\odot}$ and $\alpha = 2.3$ for $m_{\rm star} = 0.5$–$100\,{\rm M}_{\odot}$) and Pauldrach/Hillier stellar atmospheres. On the other hand, for star particles younger than 10 Myr, SUNRISE assigns a nebular spectrum that takes into account the effects of photodissociation and recombination of the surrounding gas. The nebular spectra are pre-computed with the photoionization code MAPPINGS III (Groves, Dopita & Sutherland 2004; Groves et al. 2008), and depend on the metallicity of the star particle and the gas around it, on the ISM pressure,[1] and on the photodissociation region (PDR) covering fraction $f_{\rm PDR}$. The MAPPINGS III parameters not constrained by the underlying hydrodynamical simulation, $f_{\rm PDR}$ and $M_{\rm cl}$, have been set respectively to $f_{\rm PDR} = 0.2$ and $M_{\rm cl} = 10^5\,{\rm M}_{\odot}$, following Jonsson et al. (2010).

Once a spectrum is assigned to each star particle, SUNRISE enters the radiative transfer stage, where randomly-generate photon 'packets' (rays) are propagated from these sources through the ISM using a Monte Carlo approach (we use $\sim 10^7$ Monte Carlo rays in our case[2]). It is assumed that the dust is traced by the metals with a constant dust-to-metals ratio of 0.4 (Dwek 1998), and that dust extinction is described by a Milky Way-like extinction curve normalized to $R_V = 3.1$ (Cardelli, Clayton & Mathis 1989; Draine 2003). In our model, unlike in other hydrodynamical codes where gas particles represent a mix of gas/stellar phases (e.g. Springel & Hernquist 2003), each gas particle has a single temperature, density and entropy (see Scannapieco et al. 2006 for details), and so the amount of dust is linked to the total amount of metals in the gas particle (see also Hayward et al. 2011; Snyder et al. 2013; Lanz et al. 2014).

The tracing of the rays is done on an adaptive grid, which for our simulations is represented by a number of cells between ∼30 000–400 000,[3] and covers a box with side 120 kpc, with minimum cell size of ∼220–460 pc. To compute the grid, we have assumed a value of tolerance ${\rm tol}_{\rm met} = 0.1$ and metals opacity $\kappa = 3 \times 10^{-5}\,{\rm kpc}^2\,{\rm M}_{\odot}^{-1}$ following Jonsson (2006). The broadband images in Fig. 1 show the final result of the post-processing with SUNRISE.

[1] The ISM pressure enters the MAPPINGS computation through the compactness parameter C, which is also related to the assumed cluster mass $M_{\rm cl}$ (see Groves et al. 2008; Jonsson et al. 2010).

[2] We tested the effects of increasing 10 times the number of rays, and found very small relative differences on the SEDs, the largest ones of the order of 0.2–0.3 per cent occurring for the edge-on projections, see Appendix B.

[3] We have also run SUNRISE increasing the number of cells ∼10–20 times, and found very small relative differences in the derived spectra, the largest ones occurring in the case of the edge-on SEDs, and being of the order of 0.5–1 per cent, see Appendix B.

We have also followed a simple approach by applying SPS models to derive some of the galaxy properties (see Paper I), which we discuss here when appropriate.

3 OBSERVATIONAL DATA

We compare the properties of our simulated galaxies, at redshift zero, with the SDSS data set. The SDSS camera (Abazajian et al. 2003) is designed to collect multi-colour images and spectra of a large number of objects in an area of a third of the sky, at median redshift (for galaxies) of $z \sim 0.1$. The images are taken in five different photometric bands (*u, g, r, i, z*) of increasing effective wavelength, with filter curves defined for an airmass of 1.3 at the Apache Point Observatory, pixel size of 0.396 arcsec and exposure time of 53.9 s (Gunn et al. 1998, 2006).

SDSS magnitudes are based on the AB photometric system (Oke 1965; Oke & Gunn 1983), which allows immediate conversion from magnitudes to physical fluxes (Fukugita et al. 1996). The spectrographic survey observes spectra of ∼640 target objects simultaneously, and the light of each object is collected with a single optical fibre of diameter 3 arcsec in the sky pointing at the centre of the object (see York et al. 2000; Smee et al. 2013 for a technical description, see also Paper I and Stevens et al. 2014 for a discussion of the effects of the limited fibre size on simulation properties). The wavelength covering is between 3800 and 9200Å at resolution $R = 1800$–2200, and S/N > 4 at g-mag = 20.2. In a Planck cosmology (Planck Collaboration XIII 2015), at $z \sim 0.1$, the fibre encloses a circular region of ∼5.8 kpc in diameter, sampling only ≈1/3 of the total light for a typical spiral galaxy (Brinchmann et al. 2004). The SDSS Data Release 4 (DR4; Adelman-McCarthy et al. 2006) includes an imaging catalogue of about 180 million objects and spectroscopic data of ∼850 000 objects, of which ∼565 000 are galaxies. The DR7 (Abazajian et al. 2009) contains photometric information of more than 350 million objects and spectra of ∼930 000 galaxies.

In this work, we use data sets of derived galaxy properties from the MPA-JHU analysis of SDSS DR4 (for stellar masses/ages/metallicities) and DR7 (magnitudes/colours, stellar masses, gas metallicities, SFRs). From the MPA-JHU data sets, we first select galaxies in the local universe ($z < 0.3$), and we separate the sample into early and late types according to visual classification. For the DR4 data, we use the Nair & Abraham (2010) catalogue, which includes ∼14 000 galaxies, while for DR7 we select early/late-type galaxies according to the Galaxy Zoo classification (Lintott et al. 2008, 2011), a crowdsourcing-based project of morphological classification of ≈1/3 of the SDSS DR7 galaxies. In order to better estimate how close/far from real spirals our simulated galaxies are, we further split the samples (both for DR4 and DR7) in *green valley* galaxies (Martin et al. 2007) defined according to the Salim (2014) condition on the specific star formation rate (sSFR):

$$-11.8 < \log(\mathrm{sSFR}) < -10.8 \qquad \text{(green valley)}$$

independently of the visual classification; in the figures we will plot the spiral, green valley and elliptical galaxies respectively in blue, green and red (notice that the division into separated sequences of *star-forming*, *intermediate* and *passive* galaxies is still under debate; see e.g. Casado et al. 2015). After selecting these subsets of galaxies from SDSS, the final galaxy sample that we will use consists of ∼7200 spirals, ∼700 ellipticals and ∼5700 green valley galaxies for DR4, and ∼145 000 spirals, ∼45 000 ellipticals and ∼63 000 green valley galaxies for DR7. For the sake of clarity, in the figures we will show only ∼10 per cent of these galaxies, but we will plot the contours enclosing 50 per cent and 80 per cent of objects of each type.

4 GALAXY PROPERTIES

In the next sections, we will compare the different physical properties of the simulated galaxies (magnitudes/colours, concentrations, Sérsic indices, stellar masses, mean stellar ages/metallicities, gas metallicities, SFRs) with SDSS data. For most of the galaxy properties, we will show the effects of including the observational biases in the calculation mimicking SDSS (OBS) when the galaxies are observed in the face-on projection, and the results derived directly from the simulations or with little post-processing (SIM) as commonly used in simulation studies. Furthermore, we will show the results derived using an intermediate approach, where we apply simple refinements to the SIM method that are more directly comparable to the OBS results. We have also derived the properties following the OBS method but using the edge-on projections (OBS-edge). For the different galaxy properties, we will provide linear best-fitting formulae of the relation between the OBS and SIM values, as well as between OBS and the other methods, using linear regression.

The techniques and models used to generate mock spectra from our simulated galaxies and to extract their physical properties have been described in Paper I, where we also discussed the effects of the SDSS small-aperture spectrograph (fibre bias).[4] As explained below, these are based on the conversion of the simulation's outputs into mock SEDs obtained either using an SPS model or the radiative transfer code SUNRISE. In the next sections, we will focus on showing for which properties it is more important to apply observational techniques when simulations are compared to observations, and in particular whether mimicking the biases of SDSS makes the simulations look closer to real spiral/elliptical/green valley SDSS galaxies.

4.1 Magnitudes, colours and stellar masses

In this section, we compare the position of our simulated galaxies in the colour–magnitude/colour–mass diagrams with SDSS data, showing also the changes due to the different techniques applied to calculate these quantities. In the figures, we will use the $(u - r)$ colour, as for this colour the SDSS galaxies show a clear bimodality in the colour–magnitude diagram (Strateva et al. 2001; Baldry et al. 2004). We apply the following methods to calculate the magnitudes (see also Paper I).

(i) OBS [PETRO][5]: the magnitudes are derived from SUNRISE face-on images (edge-on for the OBS-edge method) with a procedure that mimics the SDSS Petrosian magnitudes calculation (Blanton et al. 2001; Yasuda et al. 2001), i.e. extracting the Petrosian radius (Petrosian 1976) in the r band, and taking the flux inside two Petrosian radii in all bands to calculate the magnitudes. The Petrosian radius R_P is the radius that for a galaxy with luminosity profile $I(r')$ satisfies

$$\frac{\int_{0.8\,R_\mathrm{P}}^{1.25\,R_\mathrm{P}} \mathrm{d}r' 2\pi r' I(r') / [\pi(1.25^2 - 0.8^2)\, R_\mathrm{P}^2]}{\int_0^{R_\mathrm{P}} \mathrm{d}r' 2\pi r' I(r') / [\pi R_\mathrm{P}^2]} \equiv 0.2.$$

[4] The global properties are derived considering always a field of view (FoV) of 60×60 kpc, see Paper I.

[5] In the following, we give in brackets the reference labels used in Paper I when different.

The flux inside two Petrosian radii recovers nearly 98 per cent of the light for an exponential profile and ∼80 per cent for a DeVacouleur profile (Shen et al. 2003). For our galaxies, the fraction of *r*-band flux inside two Petrosian radii varies from ∼52 per cent (E-CS$^+$) to ∼100 per cent (C-MA), and is on average ∼80 per cent.

(ii) SIM [BC03]: the magnitudes of the simulations in the (*u*, *g*, *r*, *i*, *z*) bands have been calculated with the Bruzual & Charlot (2003, hereafter BC03) SPS model, assigning each stellar particle a spectrum according to its age, metallicity and mass. This is one of the most common and fast ways to calculate the spectra/magnitudes of simulated galaxies.

(iii) BC03-dust [CF00]: we add to the spectra calculated with BC03 the effects of dust extinction assuming the Charlot & Fall (2000) model (CF00). CF00 uses different extinction curves for young stellar populations (supposed to be born in dusty molecular clouds) and old ones (extincted only by dust in the ISM), without any dependence on the inclination of the galaxy.[6] The CF00 free parameters are set according to the values given in da Cunha, Charlot & Elbaz (2008), which are slightly different from the ones derived by CF00 fitting a set of star-forming galaxies; the results of the BC03-dust model then depend somehow on the values assumed for the free parameters, and cannot be considered fully predictive (see also Paper I).

For the calculation of the total stellar masses, we follow these procedures.

(i) OBS [PETRO]: the masses are derived fitting the Petrosian magnitudes in all five photometric (*u*, *g*, *r*, *i*, *z*) bands in the face-on view (edge-on in OBS-edge) to the grid of models described in Walcher et al. (2008), after subtracting nebular emission, as the fitted models include only stellar light.[7]

(ii) SIM: the total stellar mass is calculated summing the mass of star particles (within the 60×60 kpc FoV), extracted directly from the simulations' snapshots. Note that the mass in stellar particles inside two Petrosian radii in our simulations is on average ∼85 per cent of the total stellar mass in the FoV, ranging from ∼60 per cent (B-CS$^+$) to ∼100 per cent (C-MA).

In Fig. 2, we show the one-to-one relation of the SIM/BC03-dust/OBS-edge versus OBS (*r*-band) magnitudes, and the results of linear fits to the relations. From the figure, we can see that the SIM method gives in general lower (brighter) magnitudes compared to OBS, in particular for the fainter galaxies (r-mag $\gtrsim -21$), while for the brighter objects (r-mag $\lesssim -21$) it agrees better with the OBS estimation. These discrepancies are the result of the composite effect of dust extinction – dust is not considered in SIM and hence gives brighter magnitudes than OBS – and cutting the luminosity profile at $2\,R_{\rm P}$ – OBS uses the Petrosian magnitudes, further reducing the total flux (as it misses the external part of the galaxy profile, the effect being larger for galaxies with non-exponential profiles). Note that these results strongly depend on the amount of dust, the orientation (face-on/edge-on) and the luminosity profile of each galaxy. In fact, when the galaxies are seen edge-on (OBS-edge),

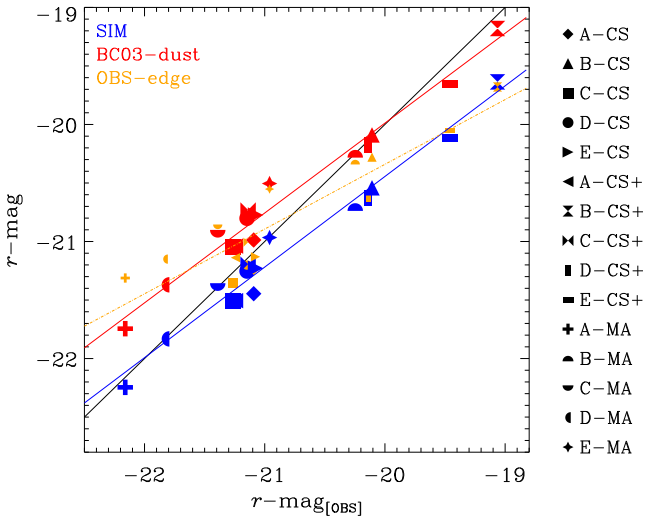

Figure 2. *r*-band absolute magnitudes of the simulated galaxies using the SIM, BC03-dust and OBS-edge methods, plotted against the observational value OBS in the one-to-one relation (black solid line). The blue, red and orange lines are, respectively, the linear fits of the SIM, BC03-dust and OBS-edge points.

the derived magnitudes are different compared to those found from the face-on images. The differences are due to the effect of dust which in general affects more the edge-on projections for dust-rich galaxies, and to the different values of the Petrosian radii, which are much higher when we see the galaxies edge-on (in particular for B-CS$^+$, D-CS$^+$ and E-CS$^+$), resulting in most of the cases in higher (i.e. fainter) magnitudes compared to OBS.

The BC03-dust model gives in most of the cases galaxies with fainter *r*-band magnitudes compared to OBS. In this case, it is important to note that BC03-dust is based on an angle-averaged dust model, from which we expect fainter magnitudes compared to the face-on magnitudes from OBS (at least for galaxies with sufficiently large $R_{\rm P}$). For galaxies of intermediate brightness, the OBS values lie in between those given by the SIM and BC03-dust methods. Note that, as explained above, the SIM and BC03-dust models give a similar slope, indicating that the shift caused by the inclusion of dust in the magnitudes of galaxies (in the range analysed here) is approximately the same for all of them.

We have performed a linear fit to the relations between the SIM/BC03-dust/OBS-edge and the OBS *r*-magnitudes, and found the following values for the slope, zero-point and correlation coefficient *R*:

$$r - \mathrm{mag}_{[\mathrm{SIM}]} = 0.77 \times \{r - \mathrm{mag}_{[\mathrm{OBS}]}\} - 4.96 \ \ [\mathrm{mag}]$$
$$R_{[\mathrm{SIM}]} = 0.986$$

$$r - \mathrm{mag}_{[\mathrm{BC03\text{-}dust}]} = 0.77 \times \{r - \mathrm{mag}_{[\mathrm{OBS}]}\} - 4.63 \ \ [\mathrm{mag}]$$
$$R_{[\mathrm{BC03\text{-}dust}]} = 0.986$$

$$r - \mathrm{mag}_{[\mathrm{OBS\text{-}edge}]} = 0.55 \times \{r - \mathrm{mag}_{[\mathrm{OBS}]}\} - 9.28 \ \ [\mathrm{mag}]$$
$$R_{[\mathrm{OBS\text{-}edge}]} = 0.911.$$

As can be seen in Fig. 2 , a linear fit is a good approximation for these relations, as quantitatively indicated by the high values of *R*. Note, however, that these relations (as well as the ones that we discuss below) somehow depend on the specific simulation code and sub-resolution model adopted, and the dependence of these

[6] We note that the BC03-dust method shifts the results of BC03 approximately by a constant factor, as the offset between different galaxies can only (slightly) change due to the different number of young star particles.

[7] To remove the nebular contribution from the broad-band magnitudes, we calculate the relative contribution of nebular emission within the fibre in each photometric band fitting the fibre spectrum with the STARLIGHT code, and assume that the relative contribution of nebular emission for the total galaxy is the same as in the fibre (see Paper I for details).

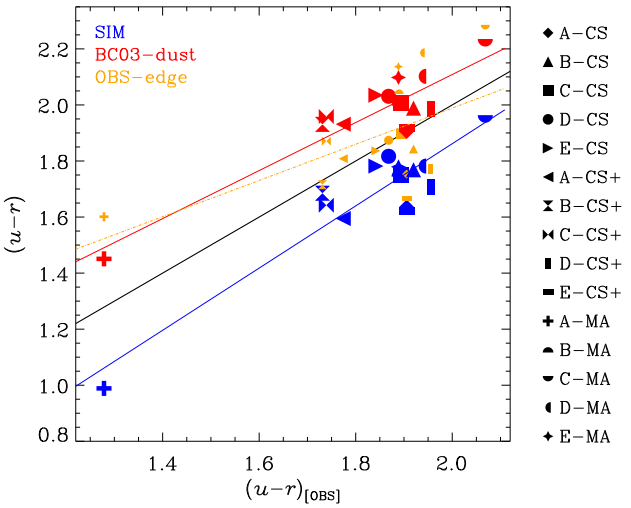

Figure 3. $(u - r)$ colours of the simulated galaxies using the SIM, BC03-dust and OBS-edge methods, as a function of the corresponding values obtained with OBS. We also show the one-to-one relation (black line) and linear fits of SIM, BC03-dust and OBS-edge (blue, red and orange lines, respectively).

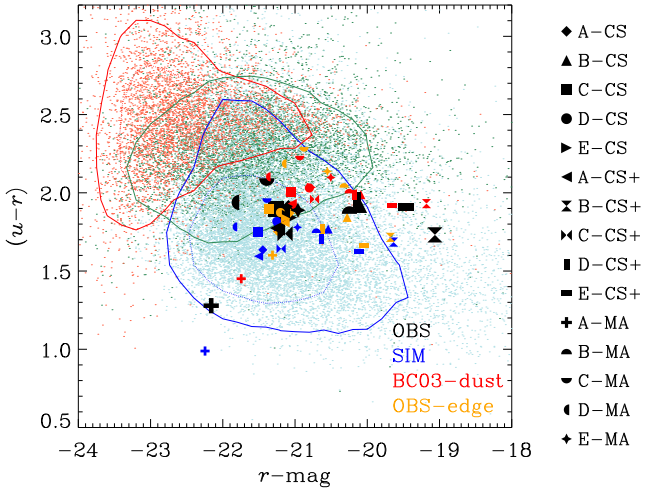

Figure 4. Colour–magnitude diagram of SDSS galaxies and simulations, using different methods to calculate the magnitudes of the simulated galaxies. In blue, green and red are the SDSS galaxies classified as spirals, green valley and ellipticals with their respective contours enclosing 50 per cent (dotted lines) and 80 per cent (solid lines) of the data points.

relations on the specific implementation of hydrodynamics has not been fully explored yet.

From Fig. 3, we see a similar behaviour for the $(u - r)$ colours of the SIM, BC03-dust and OBS-edge methods against the OBS values. The SIM method gives, as the effects of dust are ignored, bluer colours, in particular for A-MA (this is a very young and star-forming galaxy, see Sections 4.3 and 4.5). In contrast, the BC03-dust method predicts redder colours compared to OBS, as the reddening is estimated angle-averaged. Note that the use of the Petrosian magnitudes can also have an impact on the estimation of the colours, in some cases with differences reaching ∼0.1–0.2 mag (galaxies have in general different luminosity profiles/scalelengths in the different photometric bands; see e.g. Fathi et al. 2010), although the effects are strongly galaxy-dependent. The OBS-edge colours are in general redder compared to OBS, although in some cases they appear slightly bluer. This is due to the combined effect of the low amount of dust extinction and the changes in the $(u - r)$ colour due to the use of the Petrosian magnitudes.

The linear fitting functions (with respective goodness-of-fit indicators) obtained for the SIM, BC03-dust and OBS-edge results are

$$(u-r)_{[\mathrm{SIM}]} = 1.11 \times (u-r)_{[\mathrm{OBS}]} - 0.36 \ \ [\mathrm{mag}]$$
$$R_{[\mathrm{SIM}]} = 0.925$$

$$(u-r)_{[\mathrm{BC03\text{-}dust}]} = 0.86 \times (u-r)_{[\mathrm{OBS}]} + 0.40 \ \ [\mathrm{mag}]$$
$$R_{[\mathrm{BC03\text{-}dust}]} = 0.912$$

$$(u-r)_{[\mathrm{OBS\text{-}edge}]} = 0.65 \times (u-r)_{[\mathrm{OBS}]} + 0.70 \ \ [\mathrm{mag}]$$
$$R_{[\mathrm{OBS\text{-}edge}]} = 0.587.$$

Note that the slope of the fit is close to one for the SIM method, but the correlation is slightly worse compared to that found for the r-magnitudes.[8]

In Fig. 4, we show the colour–magnitude diagram of SDSS galaxies and the results obtained for our simulated galaxies using the OBS method. From the SDSS data, we select the Petrosian colours/magnitudes, making it consistent with our calculation in OBS. We also show contours for blue, red and green valley galaxies that enclose 50 per cent and 80 per cent of the corresponding data points. We find that most of the simulated galaxies are consistent with the photometrical properties of SDSS blue/green valley galaxies. A-MA is in the bluer outer part of the blue sequence, while E-CS$^+$ and B-CS$^+$ are outside of the region where most of the data are located. For comparison, we also show in this figure the results obtained with the SIM, BC03-dust and OBS-edge methods. As discussed above, using the SIM method moves the galaxies slightly down, more into the region of the blue sequence. Applying the BC03-dust model to calculate the magnitudes, the simulated galaxies move to the right (i.e. fainter magnitudes) and up (i.e. redder colours) towards the green valley region. With the OBS-edge method, the galaxies look in general slightly redder and fainter, although for most of them the position in the diagram does not change significantly.

Fig. 5 shows the colour–mass diagram, including the SDSS data points and the results of the simulations using the four methods. The results are similar to those found in Fig. 4, with most of the simulated galaxies both in the blue sequence and its intersection with the green valley when the OBS method is applied, while they move slightly down (up) using the SIM (BC03-dust/OBS-edge) technique. Note that the shift in stellar mass obtained applying the OBS method is significant for the CS sample (∼0.3 dex), as in the CS code the mass-loss of stellar particles due to stellar evolution is not well described (see Paper I). When the code includes stellar mass-loss by stars in the AGB phase (CS$^+$/MA samples), the shift in stellar mass is less important, of the order of ∼0.1–0.2 dex. Note that the main uncertainties in the observational derivation are related to

[8] The A-MA $(u - r)$ colours are far from the range covered by the rest of the galaxy sample. If we ignore this galaxy for the fits, we obtain lower correlation factors ($R \approx 0.55$–0.65) in all cases, with SIM slope and zero-point of 0.68 and 0.45, for the BC03-dust method a slope 0.63 and zero-point 0.84, and in the case of OBS-edge values of 1.10 and −0.17 for the slope and zero-point, respectively.

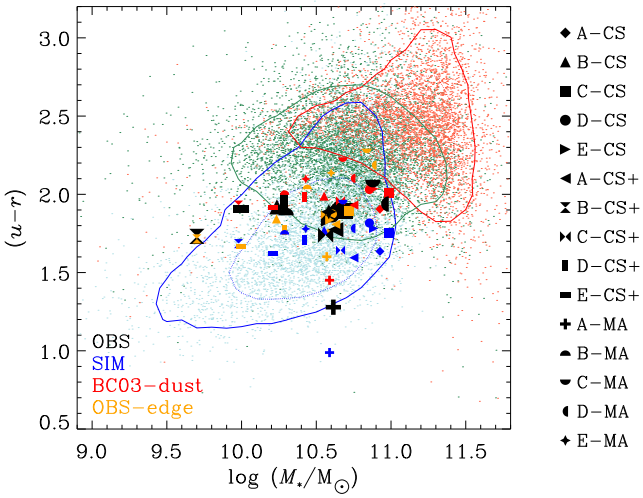

Figure 5. Colour–mass diagram of SDSS and simulated galaxies. The SIM/BC03-dust methods use the data of stellar particles of the simulation snapshots, while OBS and OBS-edge mimic the biases in the SDSS derivation of stellar mass and colours from face-on and edge-on photometric images. In blue, green and red are the SDSS galaxies classified as spirals, green valley and ellipticals with their respective 50 per cent (dotted) and 80 per cent (solid) contours.

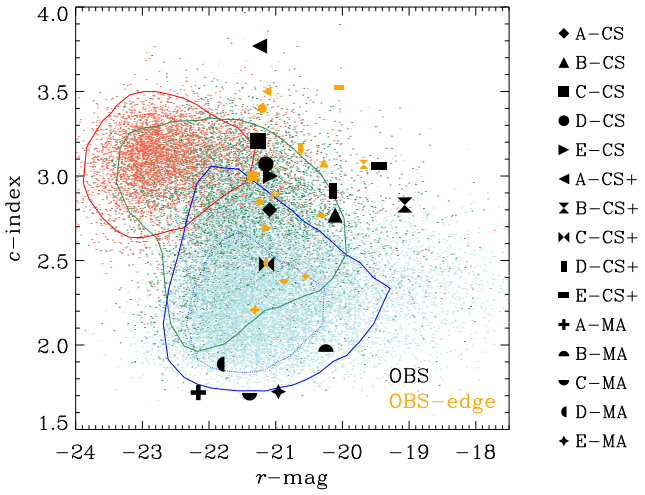

Figure 6. Concentration index c (in the r band) for SDSS galaxies and simulations, plotted versus the r-band Petrosian absolute magnitude, calculated in face-on (OBS) and edge-on (OBS-edge) projections. The dotted (solid) contours enclose 50 per cent (80 per cent) of the blue, green and red SDSS sample.

the use of the Petrosian magnitudes and to the simplified procedure to construct the grid of models used in the fit, in particular in the assumptions of star formation history (SFH) and dust attenuation (see e.g. Wuyts et al. 2009; Mitchell et al. 2013; Michałowski et al. 2014).

In summary, we find that including the observational biases has limited influence on the position of the simulated galaxies in the colour–magnitude and colour–mass diagrams. As the differences between the direct results of the simulations and those obtained mimicking the biases of SDSS data are small, the values of magnitudes and colours derived applying SPS models to simulations can be compared with observations at a good approximation (at least for old enough galaxies). Including a simple dust model to the direct result of simulations does not seem to be useful to improve the comparison with observations. The use of the different projections (face-on/edge-on) has small influence on the position of the galaxies in the colour–magnitude and colour–mass diagrams, resulting in (slightly) redder and fainter galaxies for edge-on views. Our galaxy sample looks photometrically similar to galaxies in the blue sequence/green valley, and in most of the cases is inside the range of real galaxies in the colour–magnitude and colour–mass diagrams.

The accuracy of the stellar mass determination in observations, which affects the positions of the galaxies in the colour–mass diagram, has been also investigated by several previous studies. For example, Wuyts et al. (2009) have shown that, if more filters are used when fitting the photometry, the precision in the derived stellar mass can increase up to ∼0.03–0.13 dex. On the other hand, stellar mass estimations based on fitting the SED have an accuracy of a factor of ∼2 for normal star-forming galaxies (Hayward & Smith 2015; Torrey et al. 2015), which can however be improved assuming double-component SFHs in the fitted templates (Michałowski et al. 2014). In the case of SDSS, the masses derived from the SED (correcting for the limited fibre size using the z-band luminosity) and from photometry have been shown to agree within ∼0.2 dex over the range 10^8–10^{12} $M_\odot$ (Drory, Bender & Hopp 2004).

4.2 Concentration and Sérsic index

The concentration index c (Fraser 1972; Abraham et al. 1994) is defined in SDSS as the ratio (Shen et al. 2003):

$$c = \frac{R_{90}}{R_{50}},$$

where R_{90} and R_{50} are respectively the radii including 90 per cent and 50 per cent of the total Petrosian light. The concentration index has been shown to correlate with the morphological type (Shimasaku et al. 2001), and hence is a useful tool for morphological classification in large galaxy surveys.

In Fig. 6, we show the concentration index c, calculated in the r band, as a function of the Petrosian r-band absolute magnitude, of our simulated galaxies. As these are purely observational properties, we only show the results extracted from the SUNRISE face-on (OBS) and edge-on (OBS-edge) images. From this figure, we see that the concentrations obtained using the face-on images (OBS) of the CS/CS$^+$ samples are different compared to those of the MA galaxies, the former being more concentrated than the latter – with concentration indices larger by ∼0.5–1.5. In fact, most of the CS/CS$^+$ simulations have concentrations consistent with SDSS green valley galaxies; however, some them (A-CS$^+$, B-CS$^+$, E-CS$^+$) are outside the region covered by the majority of the data points (note that two of these galaxies have concentrations in the range of observations but disagree in the magnitudes). In particular, the concentration index of A-CS$^+$ is larger than 3.7; only ≈0.07 per cent of the galaxies have concentrations above this value. On the other hand, the MA galaxies have low concentration indices and lie at the bottom of the range covered by SDSS data – only 6.5 per cent of the SDSS galaxies have concentrations below 2 where the five MA galaxies appear, and only ≈0.4 per cent below 1.8 where three of the MA galaxies lie.

The effect of the orientation on the estimated concentration indices is significant: when we use the edge-on images, the concentrations of the three samples get closer, and most of them lie in the region of the green valley/blue sequence galaxies, although the MA concentrations are in general lower than those of the CS/CS$^+$ samples. Note that the concentrations obtained from the simulations

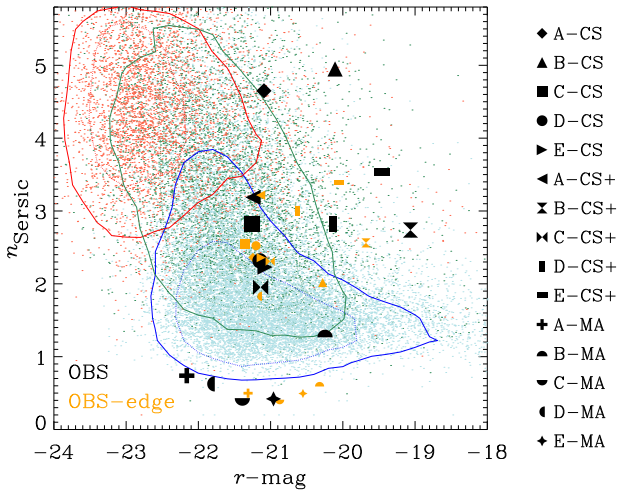

Figure 7. Sérsic indices versus absolute (Petrosian) magnitudes in the *r* band for SDSS galaxies (from Blanton et al. 2005) and simulations in face-on and edge-on views (OBS/OBS-edge respectively), together with the 50 per cent (dotted) and 80 per cent (solid) contours.

are derived considering the two extreme orientations (face-on/edge-on), while the observational sample is not corrected for inclination effects.

In Fig. 7, we plot the *r*-band Sérsic indices of the SDSS galaxies and simulations as a function of the Petrosian *r*-band magnitudes. The observational data are taken from the NYU-VAGC catalogue (Blanton et al. 2005),[9] while the Sérsic indices of the simulations have been calculated fitting a single Sérsic profile to the *r*-band face-on (OBS) and edge-on (OBS-edge) images generated with SUNRISE, using the GALFIT code (Peng et al. 2002, 2010) and assuming arbitrary axial ratio, central pixels positions and angle in the fit. In the figure, we see that the samples have different Sérsic indices; when the CS/CS$^+$ galaxies are observed face-on, they have in general indices $2 \lesssim n_s \lesssim 5$ and they lie in the region of spirals/green valley galaxies, even though some of them are somewhat outside the area covered by the data (B-CS, B-CS$^+$, E-CS$^+$), mainly in terms of the *r*-magnitudes. The MA sample has face-on indices $n_s \lesssim 1$ (hence close to an exponential profile $n_s = 1$), below the contour that includes 80 per cent of the data points of spiral galaxies. In fact, the five MA galaxies have Sérsic index $n_s < 1.4$, where less than 10 per cent of the observational data points are. Furthermore, four MA galaxies have $n_s < 0.8$, which corresponds to only 1.1 per cent of the SDSS sample.

Similarly to what we found for the concentration indices, we find that projection has an impact on the derivation of the Sérsic indices. The use of the edge-on views causes the CS/CS$^+$ galaxies to have lower values compared to those obtained from the face-on projections; as a consequence, they lie closer to the region of the green valley/blue sequence galaxies. In the case of the MA sample, the OBS-edge method predicts higher values for n_s, but the galaxies are in most of the cases still outside the 80 per cent contour of the SDSS spirals (for a discussion about the origin of these trends, see e.g. Maller et al. 2009; Pastrav et al. 2012).

Figs 6 and 7 show that *the CS/CS$^+$ and MA samples are morphologically different*, with the MA galaxies lying at the low extreme of the range of spirals both in concentration and Sérsic index when these quantities are calculated face-on, consistent with only a small fraction of the SDSS galaxies, while galaxies of the CS/CS$^+$ sample lie in the region where spirals and green valley galaxies overlap. The use of the different projections has however a significant influence on the position of the galaxies both in the concentration–magnitude and Sérsic index–magnitude diagram.

[9] Note that the Sérsic fit in the catalogue is performed on the photometric images without considering the inclination.

4.3 Stellar ages and stellar metallicities

In this section, we compare the stellar ages and metallicities of the simulated galaxies with SDSS data. The ages/metallicities in the SDSS-Garching DR4 are derived using the method described in Gallazzi et al. (2005, 2006), which is based on simultaneously fitting different absorption features adopting a Bayesian inference approach. To calculate the mean ages/metallicities in our simulations, we follow these procedures.

(i) OBS [LICK-IND-fibre]: we run SUNRISE without nebular emission and using BC03 as input stellar model;[10] we select the spectra inside a circular region of 4 kpc radius from the centre of the galaxies both in face-on (OBS) and edge-on (OBS-edge) projections, mimicking the fibre size of the SDSS spectrograph at $z \sim 0.15$ (fibre FoV). From the spectra, we measure the strength of the D4000*n*, Hβ, Hδ_A+Hγ_A, [Mg$_2$Fe] and [MgFe]$'$ absorption features (Worthey et al. 1994; Worthey & Ottaviani 1997; Balogh et al. 1999) and we compute the mean ages and metallicities fitting these indices with the method described in Gallazzi et al. (2005). As the Gallazzi et al. method is also sensitive to the estimation of the errors on the indices, from each noiseless galaxy spectrum obtained with SUNRISE we produce 1000 different spectra, adding Gaussian-distributed random noise with S/N = 10, and we measure 1000 times the strength of the absorption features for each galaxy in the two projections, using as final value for the indices and related errors, respectively, the average and standard deviation of the measurements. Note that this method to calculate the indices is different from the one presented in Paper I, as now the indices are more consistently extracted directly from the total stellar spectra, and the errors on the measurements are better estimated.[11]

(ii) SIM [SIM-fibre]: the mean ages/metallicities have been calculated averaging the (linear) ages/metallicities of stellar particles in the fibre FoV, weighted by mass as is common in simulations studies.

(iii) Lum-W-fibre [SIM-LUM-fibre]: we compute the mean ages and metallicities weighting, respectively, with the stellar particle's luminosity in the *r* band and in all SDSS bands, calculated both with BC03 and considering only particles in the region sampled by the fibre.

We plot in Fig. 8 the different estimations of the mean stellar ages of the simulated galaxies in the one-to-one relation with the value derived mimicking the SDSS observational biases, for the face-on

[10] Since the input stellar model commonly used in SUNRISE is SB99, which has sampling $\Delta\lambda \sim 20$ Å in the optical, the spectral resolution of the SED when the SB99 input spectra is used is too low to reliably measure the Lick indices. Note also that if nebular emission is neglected and the BC03 stellar model is used, the interpretation of results is more direct, as the Gallazzi et al. method assumes BC03 in the fit, and requires the subtraction of nebular emission for the calculation of the indices.

[11] In fact, there are significant differences between our new results and those of Paper I, which we discuss in Appendix A.

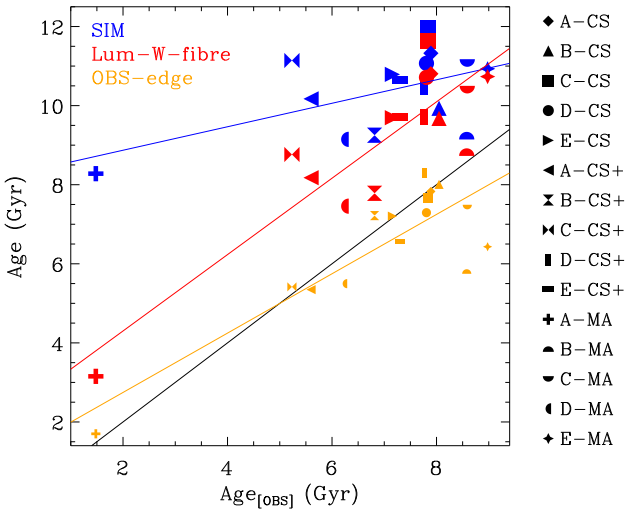

Figure 8. Mean stellar ages estimated with the different methods, plotted against the observational estimations for the face-on projection, in the one-to-one relation (black solid line).

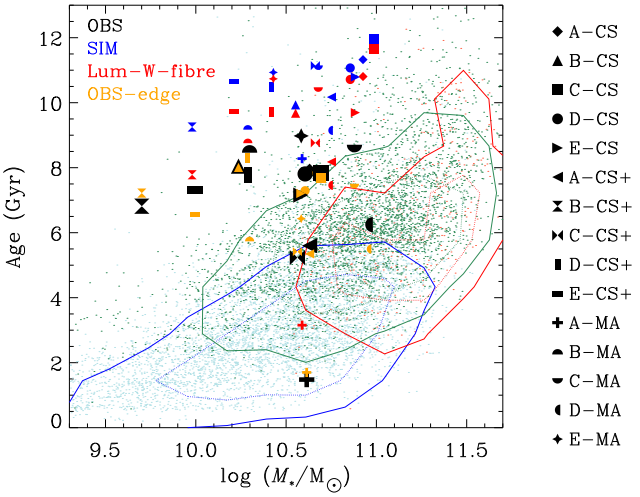

Figure 9. Stellar ages of the simulated galaxies, plotted together with SDSS data and the contours that enclose 50 per cent and 80 per cent of the data points shown respectively as dotted and solid lines.

projection (OBS). It is evident from the figure that the SIM values are systematically higher than the OBS ones, giving older stellar ages even by ∼2–4 Gyr. When the mean age is estimated weighting with the luminosity (Lum-W-fibre), we obtain younger ages compared to SIM and in better agreement with OBS, although the majority of galaxies remain older with respect to OBS by ∼1–2 Gyr. The discrepancy among the SIM and Lum-W-fibre methods tends to increase at younger ages ($\lesssim$4 Gyr); furthermore, both relations exhibit a different slope. According to the OBS age estimations, the galaxies in general appear much younger. In the case of the OBS-edge method, we obtain similar values compared to OBS, although the oldest galaxies appear slightly younger (note that the edge-on projections sample also part of the discs, which have in general a younger stellar content than the bulge). The Lum-W-fibre method gives systematically lower ages compared to SIM, as weighting with the luminosity gives more weight to the younger stellar populations, which in general emit more light than the old ones. The luminosity-weighted ages calculated with the OBS/OBS-edge methods are in general younger than Lum-W-fibre, due to the uncertainties and simplified assumptions in the procedure to construct the grid of models used to fit the Lick indices. Also note that the scatter, in particular for the SIM estimation, is relatively large, evidencing the variety of SFHs of the galaxies. It should be noted that all methods consistently consider the same set of stellar particles in the central part of the galaxies sampled by the fibre (apart from projection effects for the OBS-edge method), so the differences are not caused by the presence/strength of age/metallicity gradients (fibre bias; see Paper I), but are purely related to the different techniques applied to derive the properties.

We have made linear fits (blue/red/orange lines) to the SIM/Lum-W-fibre/OBS-edge data points obtaining the following relations and correlation factors:

$$\mathrm{Age}_{[\mathrm{SIM}]} = 0.30 \times \mathrm{Age}_{[\mathrm{OBS}]} + 8.28 \ \ [\mathrm{Gyr}]$$
$$R_{[\mathrm{SIM}]} = 0.551$$

$$\mathrm{Age}_{[\mathrm{Lum\text{-}W\text{-}fibre}]} = 0.97 \times \mathrm{Age}_{[\mathrm{OBS}]} + 2.37 \ \ [\mathrm{Gyr}]$$
$$R_{[\mathrm{Lum\text{-}W\text{-}fibre}]} = 0.884$$

$$\mathrm{Age}_{[\mathrm{OBS\text{-}edge}]} = 0.75 \times \mathrm{Age}_{[\mathrm{OBS}]} + 1.25 \ \ [\mathrm{Gyr}]$$
$$R_{[\mathrm{OBS\text{-}edge}]} = 0.850.$$

The scatter in the SIM data points is reflected in the low value of the correlation coefficient $R_{[\mathrm{SIM}]}$. As expected, a much larger correlation factor is found for the Lum-W-fibre method.

In Fig. 9, we compare the simulations' stellar ages obtained with the OBS method with mean ages from SDSS, in the stellar age–stellar mass diagram (note that the stellar mass of the OBS method is the PETRO mass estimation, Section 4.1). Our results show that about half of the simulated galaxies look older compared to the observations, and the rest is close or inside the contours corresponding to green valley galaxies (CS sample) or well inside the blue sequence (A-CS$^+$, C-CS$^+$, A-MA, D-MA) where it intersects with green valley and red galaxies. When the OBS method is applied to edge-on spectra in the fibre (OBS-edge), we obtain similar results compared to OBS, while some simulations move into the region covered by the observational data (B-MA, C-MA, E-MA). For reference, we also include in the figure results for the SIM and Lum-W-fibre methods; note that in these cases the stellar mass is calculated as the sum of the mass of stellar particles of the simulated galaxies. As discussed above, using the SIM method the galaxies appear too old compared to the observations, while weighting with the luminosity (Lum-W-fibre) moves the points down towards the range of observations, but still most of the galaxies are too old compared to the real ones.

We make a similar analysis for the mean stellar metallicities, showing in Fig. 10 the comparison among the different methods. From the figure we see that both the SIM and Lum-W-fibre methods give systematically higher metallicities compared to OBS, with the offsets increasing (up to ∼0.4–0.5 dex) for metal-poor galaxies. The discrepancy between SIM and Lum-W-fibre is explained by the different weight of old and young stars when the average metallicity is calculated weighting with the luminosity, while OBS (OBS-edge) results (for which the mean metallicity is computed luminosity-weighted) suffer from the uncertainties intrinsic in the method. When the observational method is applied to edge-on spectra, we

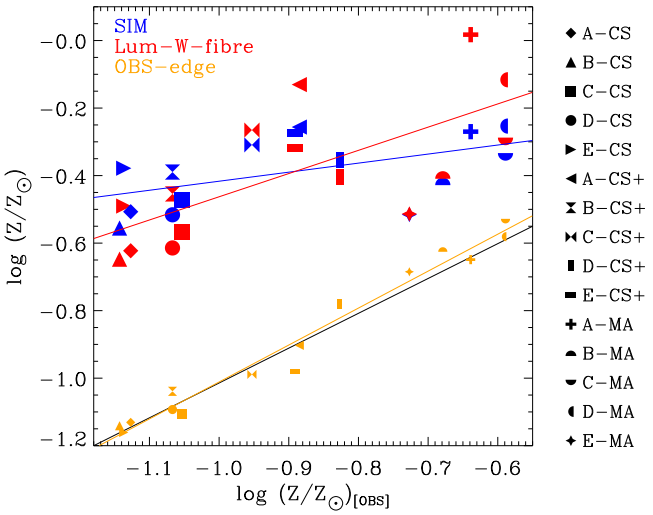

Figure 10. One-to-one relation of the different mean stellar metallicity estimations (together with the best-fitting models in blue, red and orange lines) versus the method closest to SDSS applied to face-on spectra (black line).

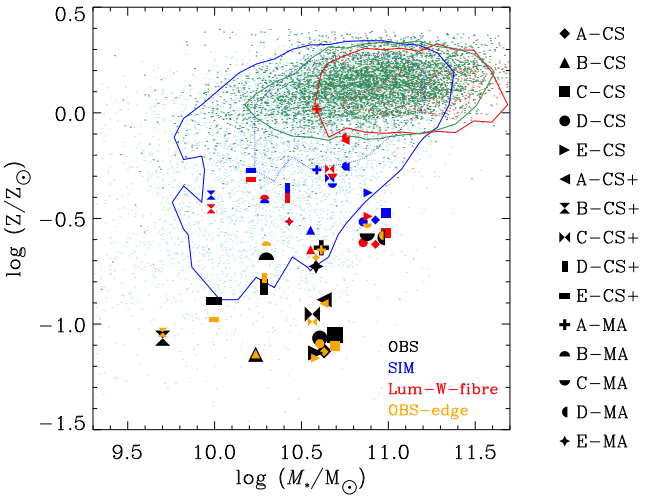

Figure 11. Mean stellar metallicity of SDSS galaxies and simulations, estimated using different techniques. The simulated galaxies appear in the area of young spirals (the blue contours contain 50 per cent and 80 per cent of SDSS spirals), but some of them are outside the range of real galaxies.

obtain very similar results compared to OBS over the full range of metallicities.

The values obtained for the linear fit and correlation coefficient are

$$\log(Z/Z_{\odot})_{[\mathrm{SIM}]} = 0.27 \times \log(Z/Z_{\odot})_{[\mathrm{OBS}]} - 0.15 \ \ [\mathrm{dex}]$$
$$R_{[\mathrm{SIM}]} = 0.525$$

$$\log(Z/Z_{\odot})_{[\mathrm{Lum\text{-}W\text{-}fibre}]} = 0.69 \times \log(Z/Z_{\odot})_{[\mathrm{OBS}]} + 0.23 \ \ [\mathrm{dex}]$$
$$R_{[\mathrm{Lum\text{-}W\text{-}fibre}]} = 0.701$$

$$\log(Z/Z_{\odot})_{[\mathrm{OBS\text{-}edge}]} = 1.1 \times \log(Z/Z_{\odot})_{[\mathrm{OBS}]} + 0.08 \ \ [\mathrm{dex}]$$
$$R_{[\mathrm{OBS\text{-}edge}]} = 0.987.$$

The correlations are similar to the ones found for the stellar ages, with the Lum-W-fibre method increasing the value of R, and the OBS-edge method having $R \sim 1$.

In Fig. 11, we show a comparison of the stellar metallicities obtained with the OBS method and observational results. We find that some of the galaxies are in the area of metal-poor spirals, while most lie outside of the region where most of the observations are (in particular the CS sample), with $\log(Z/Z_{\odot}) < -0.9$. Note that only ≈1.6 per cent of the SDSS galaxies have metallicities lower than this value. In the case of stellar metallicities derived using the SIM or Lum-W-fibre methods, galaxies appear slightly more metal-rich, with most of them lying in the blue sequence, although the CS sample is again outside the region covered by SDSS galaxies.

In conclusion, we find that the effects of using different methods to calculate the mean stellar ages/metallicities are strong and affect significantly the comparison of simulations with observations. When simple derivations of stellar ages and metallicities done in simulation studies are used, the galaxies appear older and more metal-rich compared to results obtained following observational techniques. In the case of stellar ages, the discrepancies between SIM and OBS values are large, in particular at younger ages. Weighting with the luminosity to obtain the stellar ages also affects the results, which are closer to the observational values but shifted compared to OBS by almost a constant factor. In the case of stellar metallicities, the discrepancy between SIM and OBS increases at lower metallicity, while the offset is almost constant when the mean metallicity is calculated weighting with the luminosity. The effect of the projection, estimated applying the observational method to edge-on spectra, is secondary compared to the differences arising from the use of different derivation methods. Our results show that the majority of our simulated galaxies appear older than real spirals, and with metallicities similar to or lower than the most metal-poor spirals in SDSS.

It should be noted that comparing the Lum-W-fibre and OBS results (both providing the luminosity-weighted ages/metallicities) the observational method shows a bias to systematic younger ages and lower metallicities. Notice also that our Lum-W-fibre results have a scattering with respect to the Lum-W-fibre/OBS relation of ∼0.3 dex in ages and 0.2 dex in metallicities, similar to the errors of the method estimated by Gallazzi et al. (2005) in the case of good signal-to-noise (i.e. S/N>20), namely ∼0.2 dex for the ages and ∼0.3 dex for the metallicities. In Paper I, we have shown that SED fitting methods are able to reach a higher accuracy in stellar age and metallicity determination, constraining the ages by ∼0.06 dex and the metallicities by ∼0.15–0.25 dex, although still with some trends (see Paper I); other SED fitting studies (e.g. Cid Fernandes et al. 2005) claim results similar to our findings (in the case of good S/N), with ages constrained by ∼0.08 dex and metallicities by ∼0.1 dex.

4.4 Gas metallicities

In the SDSS-Garching DR7 data set, the gas oxygen abundances (metallicities) are extracted using the method described in Tremonti et al. (2004, T04, see also Brinchmann et al. 2004), which is based on the simultaneous fit of different emission lines according to the Charlot & Longhetti (2001) model (CL01). The authors also give a calibration of the R_{23}-metallicity relation – so-called T04 calibration – which is valid on the upper branch. In this work, we derive the gas metallicities of the simulated galaxies in the following ways.

(i) OBS [T04-fibre]: the gas metallicity is calculated applying the T04 calibration to SUNRISE face-on spectra (edge-on for OBS-edge) extracted inside a circular region of 4 kpc radius at the centre of the galaxy (fibre FoV, Section 4.3), after correcting for dust extinction

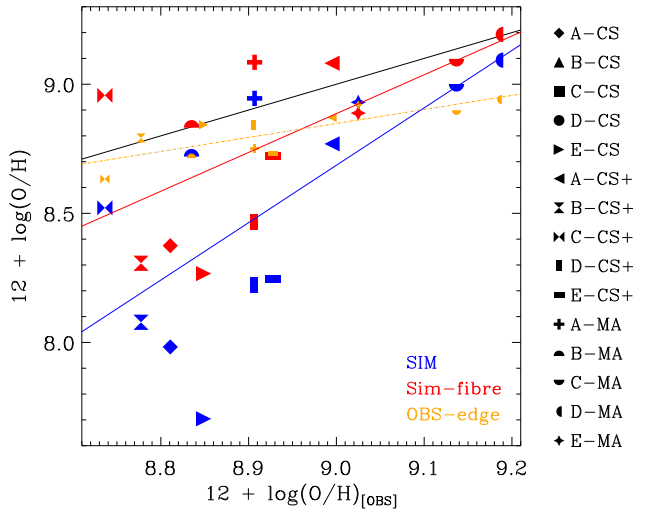

Figure 12. Comparison of the gas metallicities extracted using the different methods, in the one-to-one relation (black solid line) with the metallicity derived applying the T04 calibration to the emission line ratios of the simulated SUNRISE face-on (OBS) and edge-on (OBS-edge) spectra.

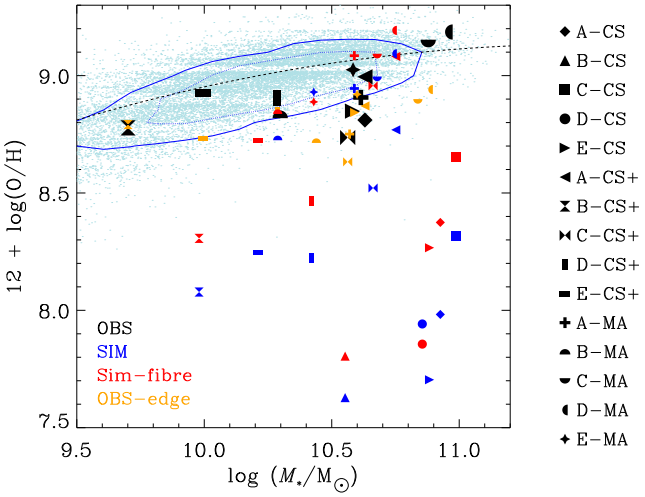

Figure 13. Mass–metallicity diagram for SDSS galaxies and simulations. The dashed line is the analytic mass–metallicity relation from Tremonti et al. (2004), while the blue contours enclose respectively 50 per cent (dotted) and 80 per cent (solid) of the data points. OBS and OBS-edge methods closely mimic SDSS biases, using the T04 calibration applied to the spectra inside the fibre FoV respectively in face-on and edge-on projections.

with the Calzetti law (Calzetti, Kinney & Storchi-Bergmann 1994). Since the T04 calibration is only valid in the upper branch of the relation, from our sample of 15 galaxies we are able to include 12 objects (11 for OBS-edge), selected according to the [N II]/[O II] ratio (Kewley & Ellison 2008).

(ii) SIM [Mass-W]: we calculate the mean $12 + \log(\mathrm{O/H})$ abundance from the oxygen/hydrogen ratio of each gas particle, weighted by the particle's mass.

(iii) SIM-fibre: the same as SIM, but only considering gas particles inside the fibre FoV in the face-on orientation.

The results of these different techniques are shown in Fig. 12, plotted in the one-to-one relation with the OBS method (T04-fibre). The plot reveals a large scatter among the methods, particularly for galaxies with $12 + \log(\mathrm{O/H}) \lesssim 9$. Deriving the metallicities with the SIM method gives in most of the cases lower values compared to OBS/SIM-fibre/OBS-edge (note that the OBS/SIM-fibre/OBS-edge methods measure the metallicity in the metal-enriched central part of the galaxies, and that our CS and CS$^+$ samples have stronger metallicity gradients compared to MA; see Paper I).

Using the SIM-fibre method moves the metallicities closer to OBS, even though with some scatter and with the tendency to underestimate the metallicity of metal-poor galaxies. Although the SIM-fibre and OBS methods sample the same central region of a galaxy, a discrepancy among the two methods is somehow expected as the emission line ratios from which the OBS values are extracted are based on the MAPPINGS III code, and the several uncertainties and assumptions on modelling nebular emission in the photoionization code may affect the derivation of the gas metallicities (see Groves et al. 2004).

The OBS-edge method gives similar results compared to OBS; however, the gas metallicity of the most metal-rich galaxies is systematically lower by 0.1–0.2 dex compared to the results when the galaxies are observed face-on (OBS). These differences may indicate that the use of a different orientation will affect the region sampled by the fibre due to projection effects, which on its turn will affect the metallicity estimation. Note also that the uncertainties in the dust corrections for edge-on/face-on galaxies may also influence the determination of the gas metallicities.

We fitted the relations between the SIM/SIM-fibre/OBS-edge and the OBS methods with linear functions (blue, red and orange lines, respectively), and obtained the following parameters:

$$12 + \log(\mathrm{O/H})_{[\mathrm{SIM}]} = 2.22 \times \{12 + \log(\mathrm{O/H})_{[\mathrm{OBS}]}\} - 11.33$$
$$R_{[\mathrm{SIM}]} = 0.674$$

$$12 + \log(\mathrm{O/H})_{[\mathrm{SIM\text{-}fibre}]} = 1.50 \times \{12 + \log(\mathrm{O/H})_{[\mathrm{OBS}]}\} - 4.65$$
$$R_{[\mathrm{SIM\text{-}fibre}]} = 0.621$$

$$12 + \log(\mathrm{O/H})_{[\mathrm{OBS\text{-}edge}]} = 0.54 \times \{12 + \log(\mathrm{O/H})_{[\mathrm{OBS}]}\} + 3.97$$
$$R_{[\mathrm{OBS\text{-}edge}]} = 0.804.$$

Note the different slopes of the relations, particularly in the case of the SIM and SIM-fibre methods, which also have a similarly low correlation factor. As expected, the relation between the OBS-edge and OBS data points has a higher correlation factor.

In Fig. 13, we compare the gas metallicities of the simulated galaxies obtained with the OBS method and the SDSS data set. We find for face-on views that most of the sample is in good agreement with the observations and inside the area covered by the data, even though the majority of the galaxies have metallicities slightly below the T04 analytical relation (dashed line), and the A/E-CS and C-CS$^+$ galaxies are outside the contour containing 80 per cent of the data. For metallicities derived from edge-on spectra, all the galaxies are below the analytic relation, and only four galaxies are inside the 80 per cent contour. Note that, in the gas metallicity–stellar mass plane, following observational techniques makes the galaxies more consistent with observations, by shifting them both in the metallicity and stellar mass values, compared to the common estimations done in simulation studies. For reference we also show results for the SIM and SIM-fibre; for SIM and SIM-fibre galaxies appear too metal-poor compared to observational data. The discrepancies are large, in some cases even by more than 1 dex. Note also that when we take into account only particles inside the fibre FoV (SIM-fibre), the metallicities of the CS/CS$^+$ samples significantly increase (while

those of the MA galaxies remain similar, since these galaxies have flatter metallicity gradients as shown in Paper I).

Our results show that to compare gas metallicities of simulated and real galaxies it is important to apply to the simulations the same methods and calibrations as in observations, in order to make the comparisons reliable. An intermediate step of obtaining a more comparable but still simple gas metallicity estimation from the simulations is to mimic the most relevant biases of the survey, in particular the SDSS fibre size. The use of face-on or edge-on views has also an influence on the gas metallicity estimation, as the fibre may sample different regions in a galaxy due to projection effects. We have shown that simple calculations obtained directly from the simulations, which neglect all the observational biases, cannot be properly compared to SDSS observations. Mimicking the SDSS derivation, our galaxies are close to the gas metallicities of spirals in SDSS, although with the trend of having oxygen abundances slightly lower than observational results. This is related to the particular calibration adopted (T04), as different studies (e.g. Kewley & Ellison 2008) have shown that the effects of the metallicity calibration used to determine the oxygen abundance are strong, affecting the determination with offsets up to ∼0.7 dex comparing theoretical (such as T04) and empirical calibrations, with the theoretical calibrations giving in general higher metallicities (see also Paper I).

4.5 Star formation rates

We analyse in this section the SFRs of our simulated galaxies, and compare them to the SDSS-Garching data. The method used to calculate the total SFRs from the SDSS spectra is described in Brinchmann et al. (2004) and is based on the CL01 model, correcting for the limited fibre size of the spectrograph with the technique described in Salim et al. (2007). For our simulated galaxies, we estimate the SFRs following these procedures.

(i) OBS [Hα]: we extract the Hα luminosity L(Hα) from the SUNRISE face-on (edge-on for the OBS-edge method) spectra that, after correcting for dust extinction with the Calzetti law using the Hα/Hβ ratio, we convert into SFR according to the Kennicutt calibration, taking into account with the factor $f_{\rm IMF} = 1.5$ the use of Kroupa/Chabrier IMF (Calzetti et al. 2009):

$$\mathrm{SFR}\ (\mathrm{M}_\odot\ \mathrm{yr}^{-1}) = 7.9/f_{\rm IMF} \times 10^{-42}\, L(\mathrm{H}\alpha)\,(\mathrm{erg\ s}^{-1}).$$

Note that this method, although different from the one used in SDSS analysis, has been shown in Brinchmann et al. (2004) to be in good agreement with it, at least for our range of stellar masses. Note also that, in addition, the method is sensitive (together with the BC03-ionizing flux) to the emission from young massive stars with lifetimes $\lesssim$10 Myr (Calzetti 2008), while the SFR derived with the SIM method is averaged over a larger time-scale (0.2 Gyr).

(ii) SIM: we calculate the SFR directly from the simulation's snapshots, considering the amount of total stellar mass formed over a certain time interval, that we set to the last 0.2 Gyr.

(iii) BC03: we convert the rate of ionizing photons $Q(\mathrm{H}^0)$ calculated with BC03 into SFR according to the calibrations given in Kennicutt (1998):

$$\mathrm{SFR}\ (\mathrm{M}_\odot\ \mathrm{yr}^{-1}) = 1.08/f_{\rm IMF} \times 10^{-53}\, Q(\mathrm{H}^0)\,(\mathrm{s}^{-1}).$$

In Fig. 14, we show the estimations of the SFR using the different methods in the one-to-one relation with the OBS results. We find in general a tight agreement among them, with scatter of the order of $\lesssim$0.2–0.4 dex, and only the lowest SFR galaxy (D-CS) has a significantly different SIM value compared to the OBS estimator.

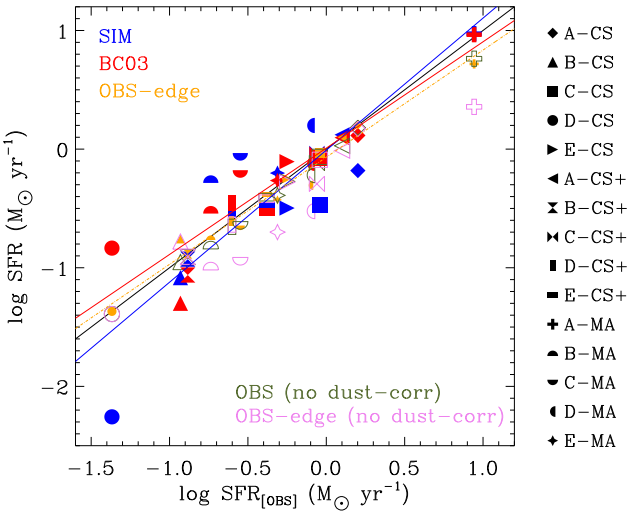

Figure 14. Comparison of the different SFR estimators, in the one-to-one relation (black line) with the observational method (OBS) based on Hα luminosity. The best fits of both SIM and BC03-ionizing flux (solid blue and red lines) are in good agreement with the relation, as well as the values derived applying the observational method in the edge-on projection (OBS-edge). The results not corrected for dust show the effect of dust extinction on the spectra for these simulations.

Projection effects do not strongly affect the derived SFRs, as evidenced by the similar relation found in the case of the OBS-edge method (note that both OBS and OBS-edge are corrected for dust extinction, and sample the full FoV of 60 × 60 kpc).

The linear functions that best fit the SIM/BC03/OBS-edge data points, and the values of the correlation factors R, are

$$\mathrm{SFR}_{[\mathrm{SIM}]} = 1.11 \times \mathrm{SFR}_{[\mathrm{OBS}]} - 0.01 \quad [\mathrm{M}_\odot\ \mathrm{yr}^{-1}]$$
$$R_{\rm SIM} = 0.871$$

$$\mathrm{SFR}_{[\mathrm{BC03}]} = 0.90 \times \mathrm{SFR}_{[\mathrm{OBS}]} + 0.01 \quad [\mathrm{M}_\odot\ \mathrm{yr}^{-1}]$$
$$R_{\rm BC03} = 0.921$$

$$\mathrm{SFR}_{[\mathrm{OBS\text{-}edge}]} = 0.90 \times \mathrm{SFR}_{[\mathrm{OBS}]} - 0.07 \quad [\mathrm{M}_\odot\ \mathrm{yr}^{-1}]$$
$$R_{\rm OBS\text{-}edge} = 0.987.$$

Note that the BC03 points appear to be in a better agreement with OBS compared to SIM, with slightly smaller scatter (i.e. higher correlation coefficient).

It is worth noting that both BC03 and OBS are based on the conversion of the rate of ionizing photons into SFR and hence sample the same time-scale of star formation, while for the SIM method we consider a much longer time-scale, as star formation is treated stochastically in the simulations. This however may result in significant discrepancies with the observational estimators, in particular in the presence of recent starbursts (Sparre et al. 2015). We have tested this effect using a time-scale of 10 Myr for the SIM method; in this case, we obtain a similar fit, with slope and zero-points of 1.103 and −0.061, respectively, but a higher correlation factor of $R_{\rm SIM} = 0.973$.

In Fig. 14, we additionally show the SFRs derived from Hα without correcting for dust, to provide a visual impression of the amount of dust extinction in our simulations, both in the face-on and edge-on projections. We see that for most of our galaxies the effects of dust are small on the face-on spectra, while dust affects

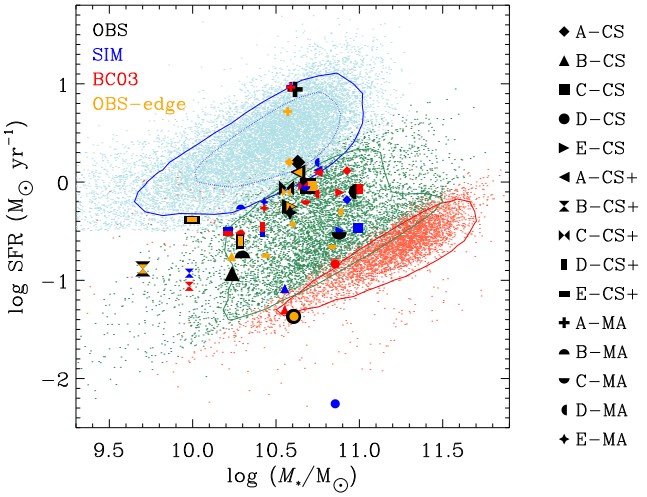

Figure 15. SFR–stellar mass diagram for SDSS and simulated galaxies, where the SDSS galaxies are shown in blue, green and red according to morphological classification, with their respective 50 per cent (dotted) and 80 per cent (solid) contours. For each simulation, we plot the results of the different methods.

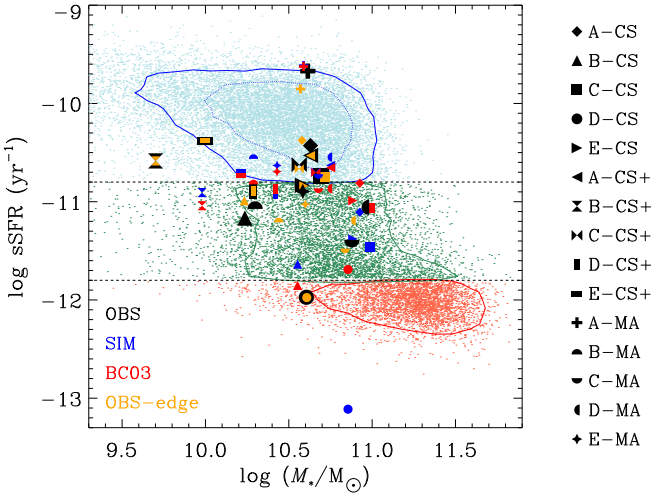

Figure 16. sSFR–stellar mass diagram showing SDSS data and the 50 per cent and 80 per cent contours of each morphological type (spirals, green valley galaxies and ellipticals respectively in blue, green and red), together with the values extracted from the simulated galaxies using different techniques.

the edge-on views more significantly, particularly for the galaxies with higher metal content (MA sample).

In Fig. 15, we compare the SFRs of simulated galaxies obtained with the OBS method to observations. The majority of the simulated galaxies have SFRs consistent with those of green valley galaxies, and only A-MA and E-CS$^+$ are in the area of the actively star-forming spirals. On the contrary, B-CS and D-CS have low SFRs, closer to the ones of red ellipticals. As shown in the previous figure, the positions of the galaxies in the SFR–stellar mass diagram when different methods are applied are similar, although in some cases the use of the OBS method (which includes the Petrosian masses) moves the simulations towards the range of real galaxies (D-CS), or from the red sequence to the green valley (e.g. B-CS) due to the different time-scales over which the SFR is derived with the OBS and SIM methods.

The sSFR diagram (Fig. 16) confirms the trends of Fig. 15, with most of the galaxies in the transition between the green valley and the blue sequence, although now more galaxies appear in the blue sequence area (note that the diagram is divided into three regions by the definition of green valley galaxies, see Section 3).

We conclude that the estimation of the SFR in simulations is not strongly affected by which method is used, and only mildly by the projection if the spectra are corrected for dust extinction; the values extracted directly from the simulations can be meaningfully compared with observations, at least for normal star-forming galaxies. Most of our simulated galaxies have SFRs at the transition between the green valley/blue sequence of SDSS galaxies. The good agreement between the SFR in simulations and the one extracted from an observational indicator such as the Hα flux is in general found for other SFR proxies, such as the [O II] line intensity (Jonsson et al. 2010) or the IR luminosity (Hayward et al. 2014; Hayward & Smith 2015), at least for quiescent star-forming galaxies.

5 DISCUSSION AND CONCLUSIONS

We have made an unbiased comparison between simulated and observed galaxies, converting the simulation outputs into synthetic observations and applying observational techniques to derive the galaxies' magnitudes, colours, stellar masses, mean stellar ages, stellar and gas metallicities and SFRs. We have used 15 hydrodynamical simulations of galaxies formed in a cosmological context adopting three different models for chemical enrichment and feedback, and we compared their properties with data from the SDSS. In order to extract the physical properties of the simulated galaxies, we first created synthetic spectra, using both an SPS model (BC03) and a full radiative transfer code (SUNRISE) to post-process the snapshots.

In a first paper of this series (Paper I), we compared the properties of the galaxies obtained applying different observational methods, and we have shown that large variations can appear, most notably in the case of the galaxies' ages and metallicities. In this paper, we focused on the methods that mimic the SDSS techniques, in order to make an unbiased comparison with the observational data set. In particular, we studied which physical properties are more affected by the observational biases that, in the case of SDSS, are mainly originated by the limited fibre size, by the methods applied to recover ages and metallicities, and by the use of the Petrosian quantities that affect both the magnitudes and stellar mass estimation.

We have given simple scalings to convert the direct results of simulations into values that can be compared with the SDSS data set in a reliable manner, although in some cases (most notably in the mean stellar ages of galaxies) the correlation has a large scatter. Moreover, the scalings we found might depend somehow on the particular hydrodynamical code we used to simulate the galaxies, which we partially tested by applying three different versions of chemical enrichment and feedback. In addition, our results are also sensitive to some choices in the derivation of the observables (e.g. inclination, as shown by the results derived in the edge-on projections), and these caveats should be taken into account when the provided scaling relations are used.

We found that the biases that appear when observational techniques are applied affect differently the various galaxy properties that we studied here. In particular, for the colours and magnitudes, mimicking observational techniques has a small effect, and the direct results of simulations can be reliably compared with SDSS data. Stellar masses derived fitting the photometry show some

discrepancies with respect to the stellar masses in simulations, although they are small except in the cases where mass-loss due to stellar evolution is not properly modelled in the hydrodynamical codes. In contrast, in the case of stellar ages and stellar and gas metallicities, the effects are stronger. For stellar ages and metallicities, the values of the simulations following observational techniques predict younger and more metal-poor galaxies compared to their mass-weighted values. The discrepancy among the methods increases both for young and for metal-poor galaxies. Refining the direct calculation by weighting with the luminosity of the stellar particles improves the mean age and metallicity determination, although strong trends with respect to the observational method appear.

For the mean oxygen abundance of the gas, we find that applying the SDSS metallicity calibration (T04) to the spectra in the fibre makes the simulated galaxies to be in much better agreement with observations compared to a direct calculation. Ignoring the fibre bias makes the galaxies appear more metal-poor, the effects being stronger for galaxies with steeper metallicity gradients. This has been already investigated in several studies (e.g. Tremonti et al. 2004; Kewley & Ellison 2008), which found that the limited fibre size strongly affects the determination of the gas metallicity and the shape of the mass–metallicity relation, particularly for galaxies with masses $M_* > 10^{10}\,\mathrm{M}_\odot$. Our findings show that, when simulated spectra are not available, the comparison of simulations' gas metallicity with SDSS data can be improved mimicking the fibre size of the SDSS spectrograph.

The determination of the SFRs is the quantity less affected by the method used, and the values extracted from the simulations and the Hα flux can be meaningfully compared (if dust extinction is correctly taken into account). We also found that the effects of the projection are significant for quantities such as the concentration and Sérsic indices, while projection has smaller effects when physical quantities are corrected for dust extinction such as in the case of gas metallicity and SFR.

Our results show that, when an unbiased comparison with the SDSS data is performed, our simulated galaxies

(i) look photometrically similar to SDSS blue/green valley galaxies;

(ii) have concentrations and Sérsic indices mostly in the range of SDSS galaxies, even though the different feedback codes give different results and in some cases outside the observed range;

(iii) are in good agreement with SDSS ages, although most of them appear older compared to SDSS spirals;

(iv) have stellar metallicities consistent with metal-poor spirals;

(v) show good agreement with observations of the gas oxygen abundances, even if they remain slightly more metal-poor;

(vi) have Hα-based SFRs in the region between the SDSS green valley galaxies and the blue sequence, although there are objects with Hα-based SFRs both in the region of strongly star-forming spirals and in the red sequence of passive ellipticals.

In summary, we have shown that a reliable comparison between observations and simulations requires in general the conversion of the direct results of simulations into observationally derived quantities taking into account the biases of the survey and mimicking its algorithms. A consistent comparison of the galaxy properties is the only possible way to reliable test the recipes for star formation, feedback and metal enrichment in hydrodynamical simulation codes.

We hope this work provides useful resources for simulators to better compare their galaxies with SDSS data, and encourages them to test the effects of applying observational techniques on the properties of the simulated galaxies. Making unbiased comparisons has been proven to be of crucial importance to decide on the success or failure of a galaxy formation model, offering insights into possible refinements of galaxy formation codes.

ACKNOWLEDGEMENTS

We thank Yago Ascasibar and Javier Casado Gómez for useful discussions and comments. We also acknowledge Michael Aumer for providing his simulations, and P.-A. Poulhazan and P. Creasey for sharing the new chemical code. GG and CS acknowledge support from the Leibniz Gemeinschaft, through SAW-Project SAW-2012-AIP-5 129, and from the High Performance Computer in Bavaria (SuperMUC) through Project pr94zo. CJW acknowledges support through the Marie Curie Career Integration Grant 303912. GG acknowledges support from the DAAD through the Spain–Germany Collaboration programme (Project ID 57050803).

REFERENCES

Abazajian K. et al., 2003, AJ, 126, 2081
Abazajian K. N. et al., 2009, ApJS, 182, 543
Abraham R. G., Valdes F., Yee H. K. C., van den Bergh S., 1994, ApJ, 432, 75
Adelman-McCarthy J. K. et al., 2006, ApJS, 162, 38
Allen J. T. et al., 2015, MNRAS, 446, 1567
Aumer M., White S. D. M., Naab T., Scannapieco C., 2013, MNRAS, 434, 3142
Bacon R. et al., 2004, in Moorwood A. F. M., Iye M., eds, Proc. SPIE Conf. Ser. Vol. 5492, Ground-based Instrumentation for Astronomy. SPIE, Bellingham, p. 1145
Baldry I. K., Glazebrook K., Brinkmann J., Ivezić Ž., Lupton R. H., Nichol R. C., Szalay A. S., 2004, ApJ, 600, 681
Baldry I. K. et al., 2012, MNRAS, 421, 621
Balogh M. L., Morris S. L., Yee H. K. C., Carlberg R. G., Ellingson E., 1999, ApJ, 527, 54
Beckwith S. V. W. et al., 2006, AJ, 132, 1729
Bellovary J. M., Holley-Bockelmann K., Gültekin K., Christensen C. R., Governato F., Brooks A. M., Loebman S., Munshi F., 2014, MNRAS, 445, 2667
Blanton M. R. et al., 2001, AJ, 121, 2358
Blanton M. R. et al., 2005, AJ, 129, 2562
Brinchmann J., Charlot S., White S. D. M., Tremonti C., Kauffmann G., Heckman T., Brinkmann J., 2004, MNRAS, 351, 1151
Bruzual A. G., 1983, ApJ, 273, 105
Bruzual G., Charlot S., 2003, MNRAS, 344, 1000 (BC03)
Bundy K. et al., 2015, ApJ, 798, 7
Calzetti D., 2008, in Knapen J. H., Mahoney T. J., Vazdekis A., eds, ASP Conf. Ser. Vol. 390, Pathways Through an Eclectic Universe. Astron. Soc. Pac., San Francisco, p. 121
Calzetti D., Kinney A. L., Storchi-Bergmann T., 1994, ApJ, 429, 582
Calzetti D., Sheth K., Churchwell E., Jackson J., 2009, in Sheth K., Noriega-Crespo A., Ingalls J., Paladini R., eds, The Fourth Spitzer Science Center Conf., The Evolving ISM in the Milky Way and Nearby Galaxies. p. 8, available at: http://ssc.spitzer.caltech.edu/mtgs/ismevol/
Cappellari M., Emsellem E., 2004, PASP, 116, 138
Cardelli J. A., Clayton G. C., Mathis J. S., 1989, ApJ, 345, 245
Casado J., Ascasibar Y., Gavilán M., Terlevich R., Terlevich E., Hoyos C., Díaz A. I., 2015, MNRAS, 451, 888
Charlot S., Fall S. M., 2000, ApJ, 539, 718
Charlot S., Longhetti M., 2001, MNRAS, 323, 887
Cid Fernandes R., Mateus A., Sodré L., Stasińska G., Gomes J. M., 2005, MNRAS, 358, 363
Colless M., 1999, Phil. Trans. R. Soc. A, 357, 105

Creasey P., Scannapieco C., Nuza S. E., Yepes G., Gottlöber S., Steinmetz M., 2015, ApJ, 800, L4
da Cunha E., Charlot S., Elbaz D., 2008, MNRAS, 388, 1595
Dalton G. et al., 2014, Proc. SPIE, 9147, 91470L
Domínguez-Tenreiro R., Obreja A., Granato G. L., Schurer A., Alpresa P., Silva L., Brook C. B., Serna A., 2014, MNRAS, 439, 3868
Draine B. T., 2003, ApJ, 598, 1017
Drory N., Bender R., Hopp U., 2004, ApJ, 616, L103
Dwek E., 1998, ApJ, 501, 643
Erb D. K., Shapley A. E., Pettini M., Steidel C. C., Reddy N. A., Adelberger K. L., 2006, ApJ, 644, 813
Fagotto F., Bressan A., Bertelli G., Chiosi C., 1994a, A&AS, 104, 365
Fagotto F., Bressan A., Bertelli G., Chiosi C., 1994b, A&AS, 105, 29
Fathi K., Allen M., Boch T., Hatziminaoglou E., Peletier R. F., 2010, MNRAS, 406, 1595
Fraser C. W., 1972, The Observatory, 92, 51
Fukugita M., Ichikawa T., Gunn J. E., Doi M., Shimasaku K., Schneider D. P., 1996, AJ, 111, 1748
Gallazzi A., Charlot S., Brinchmann J., White S. D. M., Tremonti C. A., 2005, MNRAS, 362, 41
Gallazzi A., Charlot S., Brinchmann J., White S. D. M., 2006, MNRAS, 370, 1106
García-Benito R. et al., 2015, A&A, 576, A135
Groves B. A., Dopita M. A., Sutherland R. S., 2004, ApJS, 153, 9
Groves B., Dopita M. A., Sutherland R. S., Kewley L. J., Fischera J., Leitherer C., Brandl B., van Breugel W., 2008, ApJS, 176, 438
Guidi G., Scannapieco C., Walcher C. J., 2015, MNRAS, 454, 2381 (Paper I)
Gunn J. E. et al., 1998, AJ, 116, 3040
Gunn J. E. et al., 2006, AJ, 131, 2332
Hayward C. C., Smith D. J. B., 2015, MNRAS, 446, 1512
Hayward C. C., Kereš D., Jonsson P., Narayanan D., Cox T. J., Hernquist L., 2011, ApJ, 743, 159
Hayward C. C. et al., 2014, MNRAS, 445, 1598
Hodge J. A. et al., 2013, ApJ, 768, 91
Jonsson P., 2006, MNRAS, 372, 2
Jonsson P., Groves B. A., Cox T. J., 2010, MNRAS, 403, 17
Kennicutt R. C., Jr, 1998, ARA&A, 36, 189
Kewley L. J., Ellison S. L., 2008, ApJ, 681, 1183
Kobulnicky H. A., Kewley L. J., 2004, ApJ, 617, 240
Kroupa P., 2002, Science, 295, 82
Lanz L., Hayward C. C., Zezas A., Smith H. A., Ashby M. L. N., Brassington N., Fazio G. G., Hernquist L., 2014, ApJ, 785, 39
Lintott C. J. et al., 2008, MNRAS, 389, 1179
Lintott C. et al., 2011, MNRAS, 410, 166
Madau P., Dickinson M., 2014, ARA&A, 52, 415
Maller A. H., Berlind A. A., Blanton M. R., Hogg D. W., 2009, ApJ, 691, 394
Martin D. C. et al., 2007, ApJS, 173, 415
Michałowski M. J., Hayward C. C., Dunlop J. S., Bruce V. A., Cirasuolo M., Cullen F., Hernquist L., 2014, A&A, 571, A75
Mitchell P. D., Lacey C. G., Baugh C. M., Cole S., 2013, MNRAS, 435, 87
Naab T. et al., 2014, MNRAS, 444, 3357
Nair P. B., Abraham R. G., 2010, ApJS, 186, 427
Nelson D. et al., 2015, Astron. Comput., 13, 12
Newman J. A. et al., 2013, ApJS, 208, 5
Nuza S. E., Parisi F., Scannapieco C., Richter P., Gottlöber S., Steinmetz M., 2014, MNRAS, 441, 2593
Ocvirk P., Pichon C., Lançon A., Thiébaut E., 2006, MNRAS, 365, 74
Oke J. B., 1965, ARA&A, 3, 23
Oke J. B., Gunn J. E., 1983, ApJ, 266, 713
Oppenheimer B. D., Davé R., Kereš D., Fardal M., Katz N., Kollmeier J. A., Weinberg D. H., 2010, MNRAS, 406, 2325
Pastrav B. A., Popescu C. C., Tuffs R. J., Sansom A. E., 2012, in Tuffs R. J., Popescu C. C., eds, Proc. IAU Symp. 284, The Spectral Energy Distribution of Galaxies. Cambridge Univ. Press, Cambridge, p. 306
Peng C. Y., Ho L. C., Impey C. D., Rix H.-W., 2002, AJ, 124, 266
Peng C. Y., Ho L. C., Impey C. D., Rix H.-W., 2010, AJ, 139, 2097
Petrosian V., 1976, ApJ, 209, L1
Pilbratt G. L. et al., 2010, A&A, 518, L1
Planck Collaboration XIII 2015, preprint (arXiv:1502.01589)
Salim S., 2014, Serb. Astron. J., 189, 1
JohnsonSalim S., Rich R. M., Charlot S., Brinchmann J., 2007, ApJS, 173, 267
Sánchez S. F. et al., 2012, A&A, 538, A8
Scannapieco C., Tissera P. B., White S. D. M., Springel V., 2005, MNRAS, 364, 552
Scannapieco C., Tissera P. B., White S. D. M., Springel V., 2006, MNRAS, 371, 1125
Scannapieco C., White S. D. M., Springel V., Tissera P. B., 2009, MNRAS, 396, 696
Scannapieco C., Gadotti D. A., Jonsson P., White S. D. M., 2010, MNRAS, 407, L41
Scannapieco C. et al., 2012, MNRAS, 423, 1726
Scannapieco C., Creasey P., Nuza S. E., Yepes G., Gottlöber S., Steinmetz M., 2015, A&A, 577, A3
Schaye J. et al., 2015, MNRAS, 446, 521
Shen S., Mo H. J., White S. D. M., Blanton M. R., Kauffmann G., Voges W., Brinkmann J., Csabai I., 2003, MNRAS, 343, 978
Shimasaku K. et al., 2001, AJ, 122, 1238
Skrutskie M. F. et al., 2006, AJ, 131, 1163
Smee S. A. et al., 2013, AJ, 146, 32
Smith D. J. B., Hayward C. C., 2015, MNRAS, 453, 1597
Snyder G. F., Hayward C. C., Sajina A., Jonsson P., Cox T. J., Hernquist L., Hopkins P. F., Yan L., 2013, ApJ, 768, 168
Song M. et al., 2015, ApJ, 825, 5
Sparre M., Hayward C. C., Feldmann R., Faucher-Giguère C.-A., Muratov A. L., Kereš D., Hopkins P. F., 2015, preprint (arXiv:1510.03869)
Springel V., 2005, MNRAS, 364, 1105
Springel V., Hernquist L., 2003, MNRAS, 339, 289
Springel V. et al., 2008, MNRAS, 391, 1685
Stevens A. R. H., Martig M., Croton D. J., Feng Y., 2014, MNRAS, 445, 239
Strateva I. et al., 2001, AJ, 122, 1861
Tormen G., Bouchet F. R., White S. D. M., 1997, MNRAS, 286, 865
Torrey P. et al., 2015, MNRAS, 447, 2753
Tremonti C. A. et al., 2004, ApJ, 613, 898
Vogelsberger M. et al., 2014, MNRAS, 444, 1518
Walcher C. J. et al., 2008, A&A, 491, 713
Walcher J., Groves B., Budavári T., Dale D., 2011, Ap&SS, 331, 1
Walcher C. J., Coelho P. R. T., Gallazzi A., Bruzual G., Charlot S., Chiappini C., 2015, A&A, 582, A46
Werner M. W. et al., 2004, ApJS, 154, 1
Worthey G., Ottaviani D. L., 1997, ApJS, 111, 377
Worthey G., Faber S. M., Gonzalez J. J., Burstein D., 1994, ApJS, 94, 687
Wuyts S., Franx M., Cox T. J., Hernquist L., Hopkins P. F., Robertson B. E., van Dokkum P. G., 2009, ApJ, 696, 348
Yasuda N. et al., 2001, AJ, 122, 1104
York D. G. et al., 2000, AJ, 120, 1579

APPENDIX A: STELLAR AGE AND METALLICITY DETERMINATION

In Paper I, we have used, among other methods, the Gallazzi et al. (2005) technique to determine the mean stellar ages and metallicities of the simulated galaxies. As this method is based on fitting selected Lick indices, we used the names LICK-IND and LICK-IND-fibre to refer, respectively, to the cases where we consider star particles in the full FoV and inside the fibre (figs 10–11 in Paper I). In this work (see Section 4.3), we have also used the Gallazzi et al. technique applied to the fibre spectra (referred to as LICK-IND-fibre in Figs 8–10), although the indices have been extracted from the simulations in a different way compared to Paper I, as we explain below.

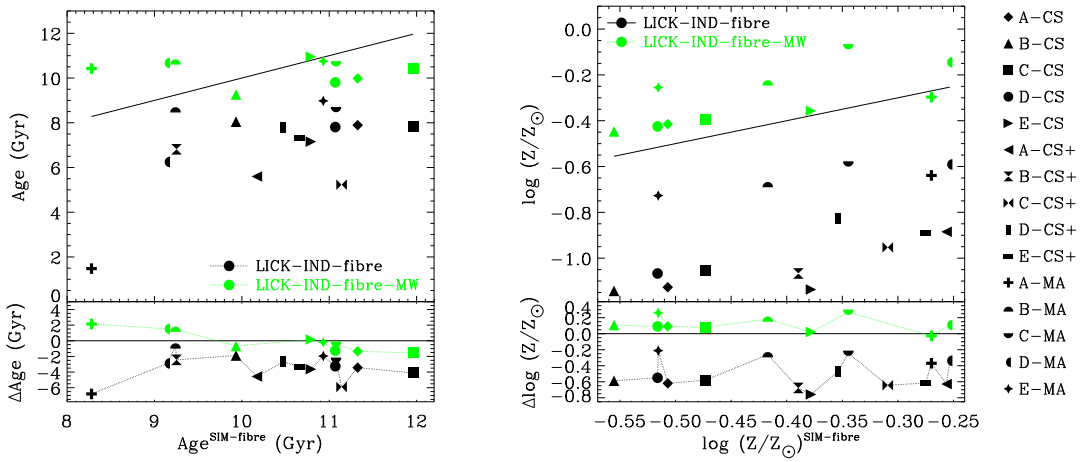

Figure A1. Mean stellar ages and metallicities calculated in the region covered by the SDSS fibre with the Gallazzi et al. (2005) method, applying two different techniques to extract the Lick indices from the simulations, in the one-to-one relation with the mean ages/metallicities taken directly from the snapshots. The LICK-IND-fibre-MW method has been used for the age and metallicity determination for 10 galaxies in Paper I, while the LICK-IND-fibre method refers to the calculations done in this work for all 15 objects.

The indices used in Paper I are estimated (for 10 galaxies) by deriving the strength of the absorption features from the BC03 tables, after interpolating the values in the tables according to the age and metallicity of each stellar particle. The averaged values of the Lick indices are obtained weighting with the particle mass and are given to the fitting routines. In contrast, in this work (see description in Section 4.3), the values of the indices are estimated from the synthetic spectra generated with SUNRISE, more consistent with the Gallazzi et al. method.

In this appendix, we make a comparison between the results for stellar ages and metallicities obtained using the two different estimations of the Lick indices. In order to avoid confusion with the naming, in this appendix we consider only the results in the fibre and we refer to the calculation done in Paper I as LICK-IND-fibre-MW, as the average values of the indices have been calculated weighting with the particle mass. The names LICK-IND-fibre are then kept for the estimations done using the techniques described in this work.

In Fig. A1, we show the mean stellar ages and metallicities obtained using the Lick indices method, as a function of the age/metallicity derived directly from the simulations (SIM). The upper panel of each figure shows the results of the 1:1 relation, while the lower panel shows the corresponding differences (note that these figures are similar to figs 10–11 of Paper I, but only including the Gallazzi et al. determination).

From the figures it is evident that the determination of a galaxy's stellar age and metallicity strongly depends on the way the indices are calculated in the simulated galaxies; for stellar ages (on the left), the discrepancies between the LICK-IND-fibre and LICK-IND-fibre-MW methods are significant and increase at younger ages, with the former giving systematically younger ages compared to the latter. The two methods agree better for ages $\gtrsim$ 10 Gyr, although the MW calculation still predicts galaxies older by ∼2–4 Gyr. It is important to note that while the MW calculation predicts galaxies that look older at younger ages and slightly younger at older ages ($\gtrsim$ 10 Gyr) compared to the SIM values, the calculations used in this work always predict younger galaxies compared to SIM, without any strong dependence on the mean stellar age.

From the right figure (mean metallicity), we again see differences between the metallicity determination obtained with the two estimations of the Lick indices. In particular, the use of the MW method gives systematically higher metallicities compared to LICK-IND, even by ∼1 dex, without strong dependence on the metallicity. Finally, we note that the MW estimation is in better agreement with the SIM values, at least for metal-rich galaxies, although it predicts in general slightly higher metallicities, while the LICK-IND results exhibit the opposite trend, with systematically lower metallicities with respect to SIM.

APPENDIX B: TESTING THE DEPENDENCE OF THE OBSERVABLES ON SUNRISE FREE PARAMETERS

In this appendix, we explore the robustness of our results on the change of the SUNRISE free parameters. We have in particular

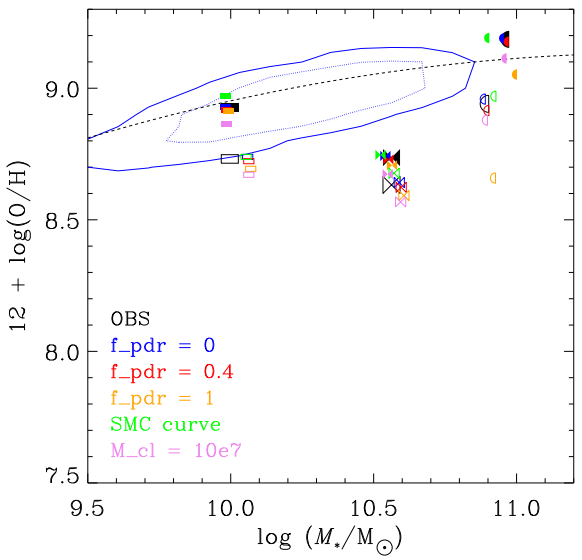

Figure B1. Gas metallicity extracted using the T04 calibration applied to SUNRISE spectra of three simulated galaxies, computed using different values for $f_{\rm PDR}$, $M_{\rm cl}$ and an SMC-like dust extinction curve. In filled and open symbols we show, respectively, the quantities computed face-on and edge-on, with the OBS symbols giving the results used in this work.

tested the dependence of the physical properties recovered by the observational methods on the choice of the MAPPINGS parameters $f_{\rm PDR}$ and $M_{\rm cl}$, and on the assumed dust extinction curve in SUNRISE. We re-run SUNRISE for three simulated galaxies, assuming three different values for $f_{\rm PDR}$ $\{0, 0.4, 1\}$ and $M_{\rm cl} = 10^7\,{\rm M}_\odot$ (while in this work we have assumed $f_{\rm PDR} = 0.2$ and $M_{\rm cl} = 10^5\,{\rm M}_\odot$).

We found that the most relevant effects on the magnitude and colour arise by the use of a Small Magellanic Cloud (SMC) dust curve, however with small differences $\lesssim$0.05–0.15 mag in the *r*-band magnitude and 0.05–0.2 mag in the $(u - r)$ colour. The effect on the stellar mass is in most of the cases negligible, lower than $\lesssim$0.05 dex. The SMC dust curve also affects the concentrations, with differences of the order of $\lesssim$0.02, and the Sérsic index determination changing the results by $\lesssim$0.1, while the effects of the other parameters are negligible on these two quantities. On the contrary, the gas metallicity is the physical quantity more sensible to the changes in the free parameters (Fig. B1), the strongest effects arising by the choice of $f_{\rm PDR}$ (especially for $f_{\rm PDR} = 1$) and $M_{\rm cl}$, although in general the differences are $\lesssim$0.1 dex. The SFR and sSFR are only slightly affected by the changes in the parameters, with offsets of the order of $\lesssim$0.1–0.2 dex.

This paper has been typeset from a TEX/LATEX file prepared by the author.